



**HAL**  
open science

## **Thermal attenuation and lag time in fractured rock: theory and field measurements from joint heat and solute tracer tests**

Jérôme de La Bernardie, Olivier Bour, Tanguy Le Borgne, Nicolas Guihéneuf,  
Eliot Chatton, Thierry Labasque, Hugo Le Lay, Marie-Françoise Gerard

### ► **To cite this version:**

Jérôme de La Bernardie, Olivier Bour, Tanguy Le Borgne, Nicolas Guihéneuf, Eliot Chatton, et al.. Thermal attenuation and lag time in fractured rock: theory and field measurements from joint heat and solute tracer tests. *Water Resources Research*, 2018, 54 (12), pp.10053-10075. 10.1029/2018WR023199 . insu-01923664

**HAL Id: insu-01923664**

**<https://insu.hal.science/insu-01923664>**

Submitted on 18 Feb 2019

**HAL** is a multi-disciplinary open access archive for the deposit and dissemination of scientific research documents, whether they are published or not. The documents may come from teaching and research institutions in France or abroad, or from public or private research centers.

L'archive ouverte pluridisciplinaire **HAL**, est destinée au dépôt et à la diffusion de documents scientifiques de niveau recherche, publiés ou non, émanant des établissements d'enseignement et de recherche français ou étrangers, des laboratoires publics ou privés.



## Water Resources Research

### RESEARCH ARTICLE

10.1029/2018WR023199

#### Key Points:

- We present expressions for thermal lag time and attenuation coefficient, quantifying the impact of flow channeling on heat transfer in fractured media
- Joint solute and thermal tracer tests support analytical results and provide new constraints on fracture aperture and flow topology
- Single-well thermal tracer tests offer an alternative to cross-borehole thermal tracer tests for characterizing thermal transport in the field

#### Correspondence to:

J. de La Bernardie,  
jerome.la.bernardie@gmail.com

#### Citation:

de La Bernardie, J., Bour, O., Le Borgne, T., Guihéneuf, N., Chatton, E., Labasque, T., et al. (2018). Thermal attenuation and lag time in fractured rock: Theory and field measurements from joint heat and solute tracer tests. *Water Resources Research*, 54, 10,053–10,075. <https://doi.org/10.1029/2018WR023199>

Received 29 APR 2018

Accepted 1 NOV 2018

Accepted article online 12 NOV 2018

Published online 17 DEC 2018

## Thermal Attenuation and Lag Time in Fractured Rock: Theory and Field Measurements From Joint Heat and Solute Tracer Tests

J. de La Bernardie<sup>1</sup> , O. Bour<sup>1</sup>, T. Le Borgne<sup>1</sup> , N. Guihéneuf<sup>1,2</sup> , E. Chatton<sup>1</sup>, T. Labasque<sup>1</sup>, H. Le Lay<sup>1,3</sup>, and M.-F. Gerard<sup>1</sup>

<sup>1</sup>Université de Rennes, CNRS, Géosciences Rennes-UMR 6118, Rennes, France, <sup>2</sup>G360 Institute for Groundwater Research, College of Engineering and Physical Sciences, University of Guelph, Ontario, Canada, <sup>3</sup>UMR SAS, Agrocampus Ouest INRA, Rennes, France

**Abstract** The modeling and prediction of heat transfer in fractured media is particularly challenging as hydraulic and transport properties depend on a multiscale structure that is difficult to resolve. In addition to advection and dispersion, heat transfer is also impacted by thermal attenuation and lag time, which results from fracture-matrix thermal exchanges. Here we derive analytical expressions for thermal lag time and attenuation coefficient in fractured media, which quantify the effect of fracture geometry on these key factors. We use the developed expressions to interpret the results of single-well thermal and solute tracer tests performed in a crystalline rock aquifer at the experimental site of Ploemeur (H+ observatory network). Thermal breakthrough was monitored with fiber-optic distributed temperature sensing (FO-DTS), which allows temperature monitoring at high spatial and temporal resolution. The observed thermal response departs from the conventional parallel plate fracture model but is consistent with a channel model representing highly channelized fracture flow. These findings, which point to a strong reduction of fracture-matrix exchange by flow channeling, show the impact of fracture geometry on heat recovery in geothermal systems. This study also highlights the advantages to conduct both thermal and solute tracer tests to infer fracture aperture and geometry.

### 1. Introduction

The transport of heat in fractured media is a key process in a range of environmental and industrial applications (Bense et al., 2016; Guo et al., 2016), including geothermal energy production (Axelsson et al., 2001; Olasolo et al., 2016; O'Sullivan et al., 2001), aquifer thermal energy storage (Kim et al., 2010; Molson et al., 1992), and hydrothermal flows (Curewitz & Karson, 1997; Malkovsky & Magri, 2016; Person et al., 2012). Furthermore, heat is increasingly used as a tracer of hydrological processes (Anderson, 2005; Burns et al., 2016; Manga & Kirchner, 2004; Saar, 2011; Somogyvari et al., 2016), in particular in the context of fractured media (Cherubini et al., 2017; Hawkins et al., 2017; Klepikova et al., 2016). In this regard, the development of distributed fiber optic temperature sensing methods is currently broadening the range of possibilities for extracting new information from high-resolution monitoring of temperature in space and time (Bense et al., 2016; Read et al., 2013).

In the context of geothermal energy, shallow porous aquifers are conventionally used to achieve periodic heating and cooling or to store energy produced by solar panels through geothermal doublets (Banks, 2009; Molz et al., 1978; Sauty et al., 1982) or standing column wells (Pasquier et al., 2016; Rode et al., 2015; Woods & Ortega, 2011). However, such applications in shallow crystalline rocks are more challenging mainly due to the time required for conduction in rock matrix, the spatial variability of hydraulic properties, and the relatively low permeability of the rocks (Axelsson et al., 2001; Berkowitz, 2002; de La Bernardie et al., 2019; Neuman, 2005). Nevertheless, the presence of natural or induced transmissive fractures may locally allow fluid circulation, which thermally interact with the surrounded matrix and facilitate heat storage or extraction (Axelsson et al., 2001). For deeper geothermal energy exploitation through enhanced geothermal systems, hydraulic stimulation is usually needed, as fractures are generally not transmissive enough to allow fluid circulation between boreholes (Gerard et al., 2006; Haring et al., 2008; Menberg et al., 2016; Olasolo et al., 2016). The understanding of thermal behavior of geothermal systems in fractured media is still challenging. The

characterization of thermal transport in fractured rocks through thermal tracer experiments and modeling is thus essential to predict and optimize geothermal system efficiency.

During joint solute and thermal transport in an aquifer, a thermal plume is expected to slow down with respect to a solute plume. This thermal lag time occurs simultaneously with a thermal attenuation due to thermal exchanges by conduction between the liquid and solid phases and to the fact that thermal diffusivity is orders of magnitude higher than solute diffusion. Here we assume that within the fracture, advection usually prevails on water thermal diffusivity, so that, thermal lag time is poorly influenced by conduction in water compared to conduction in rock. In porous media, local thermal equilibrium between the fluid and the solid phase can be assumed as the characteristic conduction time of heat into the solid grain is small (Shook, 2001). Hence, heat transport can be modeled by simply rescaling the effective velocity in the advection-dispersion equation by the thermal retardation factor:

$$R_T = \frac{(1 - \phi)\rho_g c_g}{\phi\rho_w c_w} \quad (1)$$

where  $\phi$  is the porosity,  $\rho_g$  and  $c_g$  are the density ( $\text{kg/m}^3$ ) and specific heat capacity ( $\text{J} \cdot \text{kg}^{-1} \cdot \text{K}^{-1}$ ) of the grains, and  $\rho_w$  and  $c_w$  are the density ( $\text{kg/m}^3$ ) and specific heat capacity ( $\text{J} \cdot \text{kg}^{-1} \cdot \text{K}^{-1}$ ) of water. In fractured media, local thermal equilibrium cannot be generally assumed since the characteristic time of conduction in the matrix block can be very long and is often larger than the times of interest. Hence, thermal transport cannot be simulated by a simple advection-dispersion equation with rescaled effective velocity as in porous media and the role of fracture/matrix exchanges has to be explicitly taken into account. Luhmann et al. (2015) have derived semianalytical expressions for thermal lag time and attenuation coefficient in karst conduits and analyzed the effect of conduit geometry (parallel plate or cylindrical conduit). However, these derivations rely on a separation of the temporal and spatial variables, which limits its applicability to sinusoidal inputs. As discussed in the present study, for a general input, the matrix temperature is a temporal convolution of temperature in the fracture and the temporal and spatial variables are fully coupled (e.g., Carrera et al., 1998).

Simulation of thermal transport in fractured media requires complexity reduction, which is often achieved by assuming simplified fracture network geometries including a single or few homogeneous fractures (Bodvarsson & Tsang, 1982; Gringarten et al., 1975; Heuer et al., 1991; Lauwerier, 1955; Molson et al., 2007; Ruiz Martinez et al., 2014).

Yet several numerical (Geiger & Emmanuel, 2010; Guo et al., 2016; Neuville et al., 2010) and experimental (Hawkins et al., 2017; Klepikova et al., 2016; Pastore et al., 2018) studies have shown that flow channeling has a significant impact on heat transfer properties. In particular, Neuville et al. (2010) have observed that flow channeling induces a reduction of thermal exchanges between fluid and matrix due to the increase of flow velocity and reduction of transit times in the channeled areas. Furthermore, Klepikova et al. (2016) have shown that flow channeling increases thermal exchanges between the fluid and the rock as radial conduction from the channel to the matrix is more efficient for thermal transfer than linear conduction in the parallel plate model. Thus, flow channeling appears to have two antagonist effects on heat transfer: on the one hand, it reduces the time of contact of the fluid with the rock, hence reducing heat transfer; on the other hand, it can enhance locally heat transfer by increasing the dimensionality of the diffusive flux. Here we develop a general framework that quantifies the joint effect of these two mechanisms on thermal attenuation and lag time.

We present analytical expressions for thermal lag time and attenuation coefficient in fractured media for different fracture geometries and flow fields. Thermal lag time is defined from the delay of thermal breakthrough curves with respect to reference solute breakthrough curves, and the thermal attenuation coefficient is the decline of the peak of the thermal breakthrough curve with respect to the injected temperature. From field data obtained using a novel single-well thermal and solute tracer tests setup, we show that the proposed analytical framework provides a powerful tool for interpreting joint solute and thermal tracer tests and infer information on flow topology and heat transfer in fractured media. In the following, we first present the analytical developments. We then describe the field site, the experimental setup, the instrumentation, and the data processing, which allows the acquisition of high precision temperature records. In a fourth section, thermal breakthrough curves are described, compared with solute breakthrough curves, and modeled with the analytical framework developed here.

## 2. Analytical Expressions for Thermal Lag Time and Attenuation Coefficient in Fractured Media

The conventional thermal retardation factor expression (equation (1)), which assumes local thermal equilibrium between the fluid and solid phases, is generally inapplicable to fracture rocks. However, thermal lag time and attenuation coefficient may be defined from the characteristic time and amplitude of a thermal breakthrough curve. In this section, we develop analytical expressions for thermal lag time and attenuation coefficient in fractures modeled as planes (Figure 1a) or channels referring to cylindrical channels (Figure 1b), which are end-member representations of homogeneous and highly channelized fractures (Klepikova et al., 2016). Note that the equations and memory functions used for developing those expressions have been used in previous studies (Carrera et al., 1998; Haggerty et al., 2000; Klepikova et al., 2016; Zhou et al., 2017). We recall the corresponding derivations here for completeness since they allow a full understanding of the expressions derived for the thermal time lag and attenuation coefficient.

### 2.1. Theoretical Framework

We consider a double porosity media where flow is localized in fractures and thermal conduction occurs in the surrounding impervious infinite rock matrix. To simplify the analytical developments of thermal lag time and attenuation coefficient, we follow the classical assumptions of Bodvarsson and Tsang (1982), Gringarten et al. (1975), Lauwerier (1955), and Tang et al. (1981) for fracture-matrix transport problems. In the fracture, we assume that diffusion induces complete mixing in the fracture width. In the matrix, we assume that heat diffusion occurs dominantly in the direction perpendicular to the fracture walls. We thus neglect heat conduction parallel to the fracture walls. Ruiz Martinez et al. (2014) have shown that this assumption may impact thermal breakthrough during diffusion-dominated and/or long-term experiments. The theoretical framework developed here is thus applicable when the observation times are smaller than the characteristic diffusion times in the matrix. To simplify the derivation of analytical expressions of thermal retardation coefficient and lag time, we neglect thermal dispersion in the fracture. This provides a general theoretical framework for studying the effect of fracture geometry on heat transport. For modeling jointly the full solute and heat tracer breakthrough curves, we relax this assumption and consider also thermal dispersion (Becker & Shapiro, 2000; Welty & Gelhar, 1994), which allows for a better fit of the first arrival time and peak, as discussed in the section 4.4.

Under these assumptions, thermal transport in the fracture and the matrix is described by (Carrera et al., 1998; Klepikova et al., 2016)

$$\rho_w c_w \frac{\partial T_f}{\partial t} = -\rho_w c_w u \nabla T_f - F_m, \quad (2)$$

$$F_m = \lambda_m \sigma_m (\eta = 0) \frac{\partial T_m}{\partial \eta} \Big|_{\eta=0} \quad (3)$$

and

$$\sigma_m(\eta) \rho_m c_m \frac{\partial T_m}{\partial t} = \frac{\partial}{\partial \eta} \left( \sigma_m(\eta) \lambda_m \frac{\partial T_m}{\partial \eta} \right), \quad (4)$$

where  $T_f$  and  $T_m$  are respectively the fracture and matrix temperature anomaly (relative to the background temperature  $T_0$ ),  $u$  is the flow velocity in the fracture (m/s),  $F_m$  is the specific heat flux from the fracture to the matrix ( $\text{W}/\text{m}^3$ ),  $\eta$  is the depth into the matrix from fracture wall (m),  $\lambda_m$  is the thermal conductivity of matrix ( $\text{W} \cdot \text{m}^{-1} \cdot \text{K}^{-1}$ ),  $\rho_m$  is the density of matrix,  $c_m$  is the specific heat capacity of matrix ( $\text{J} \cdot \text{kg}^{-1} \cdot \text{K}^{-1}$ ) and  $\sigma_m$  is the specific surface area of matrix that accounts for the matrix geometry ( $\text{m}^{-1}$ ) where  $\sigma_m(\eta) = 2/a$  for the planar fracture and  $\sigma_m(\eta) = 2(a + \eta)/a^2$  for the channel.

Initial and boundary conditions of equation (2) and (4) are

$$T_m(x, \eta, t = 0) = T_f(x, t = 0) = 0, \quad (5)$$

$$T_f(x = 0, t) = S(t), \quad (6)$$

$$T_m(x, \eta = 0, t) = T_f(x, t), \quad (7)$$

$$\frac{\partial T_m}{\partial \eta}(x, \eta = \infty, t) = 0. \quad (8)$$

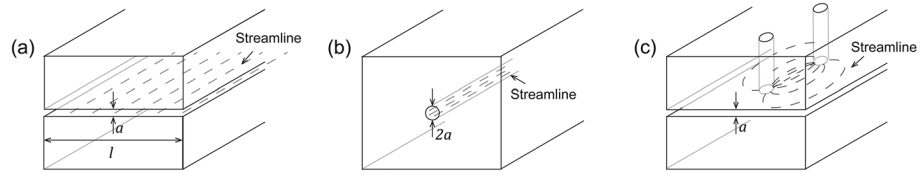


**Figure 1.** 3-D illustrations of the different fracture geometries with (a) a parallel plate finite fracture in linear flow field, (b) a channel in a linear flow field, and (c) a parallel plate fracture in a dipole flow field. The  $a$  is the fracture aperture for the parallel plate fracture model and the radius for the channel model. The  $l$  is the fracture width.

where  $x$  is the coordinate along the fracture (m) and  $S(t)$  is a source term describing the thermal tracer injection.

## 2.2. Analytical Solution in Laplace Transform

Equations (2) to (4), subjected to the boundary conditions (5) to (8) can be solved by expressing the matrix temperature as a convolution of the fracture temperature (Carrera et al., 1998; Klepikova et al., 2016):

$$T_m(x, \eta, t) = \int_0^t dt' G(\eta, t - t') T_f(x, t') = G * T_f, \quad (9)$$

where  $G(\eta, t)$  is the Green's function ( $s^{-1}$ ), which solves (4) for the boundary condition  $G(\eta = 0, t) = \delta(t)$ . Integrating equation (4) in space, one obtains the specific heat flux from the fracture to the matrix,

$$F_m = \frac{\partial}{\partial t} \int_0^\infty d\eta \rho_m c_m \sigma_m(\eta) T_m(x, \eta, t) = \frac{\partial}{\partial t} \int_0^t dt' \int_0^\infty d\eta \rho_m c_m \sigma_m(\eta) G(\eta, t - t') T_f(x, t'). \quad (10)$$

Defining  $\varphi$  as the memory function ( $s^{-1}$ )

$$\varphi(t) = \int_0^\infty d\eta \sigma_m(\eta) G(\eta, t), \quad (11)$$

we obtain

$$F_m = \rho_m c_m \frac{\partial}{\partial t} (\varphi * T_f) = \rho_m c_m \varphi * \frac{\partial}{\partial t} T_f. \quad (12)$$

Inserting (12) in (2), the Laplace transform of (2) leads to (Barker, 2010; Carrera et al., 1998)

$$-u \nabla \bar{T}_f + p(1 + \sigma \bar{\varphi}) \bar{T}_f = 0, \quad (13)$$

where the overbar expresses Laplace transformation,  $p$  is the Laplace variable, and  $\sigma = \rho_m c_m / \rho_w c_w$  is the ratio of matrix to fracture thermal storage. The solution of equation (13) for a Dirac source  $S(t) = \Delta T_i \Delta t_i \delta(t)$  in a linear flow field (where the experimental temperature increase  $\Delta T_i$  and the experimental time scale  $\Delta t_i$  depend on the experimental conditions) is thus (Barker, 2010; Carrera et al., 1998)

$$\bar{T}_f(p) = \Delta T_i \Delta t_i e^{-pt} e^{-pt\sigma(1+\sigma\bar{\varphi})}, \quad (14)$$

where  $t_a$  is the advective transit time in the fracture (s). From this solution, Barker (2010) also developed the solution of equation (13) for an instantaneous source in a dipole flow field, which will be useful for the present study (see Appendix A).

## 2.3. Expression of the Thermal Lag Time and Attenuation Coefficient for Different Geometries and Flow Fields

To propose a general formulation for the thermal lag time  $\tau_{th}$  and attenuation coefficient  $d_{th}$ , we define them from the thermal transfer function, which is independent of the injection condition. For a given injection

temperature anomaly in the fracture  $T_f(t)$ , the transfer function at a position  $x$  in the fracture is defined in the Laplace domain as

$$\bar{h}(x, p) = \frac{\bar{T}_f(x, p)Q}{\bar{T}_i(p)Q_i}, \quad (15)$$

where  $Q$  and  $Q_i$  are respectively the pumping flow rate and the injection flow rate ( $\text{m}^3 \cdot \text{s}^{-1}$ ). For a pulse injection  $T_f(t) = \Delta T_i \Delta t_i \delta(t)$ , the transfer function is

$$h(x, t) = \frac{Q}{Q_i \Delta T_i \Delta t_i} T_f(x, t). \quad (16)$$

For a continuous injection  $T_f(t) = \Delta T_i H(t)$ , where  $H(t)$  is the Heaviside function, the transfer function is

$$h(x, t) = \frac{Q}{Q_i \Delta T_i} \frac{\partial T_f(x, t)}{\partial t}. \quad (17)$$

We define the thermal lag time  $\tau_{th}$  from the peak time  $t_{peak}$  (s) of the thermal transfer function

$$\tau_{th} = t_{peak} - t_a, \quad (18)$$

where  $t_a$  is the characteristic advection time determined from the peak of a solute transfer function obtained under the same condition and the thermal attenuation coefficient  $d_{th}$  ( $\text{s}^{-1}$ ) is the maximum amplitude of the thermal transfer function  $h$ :

$$d_{th} = h(t_{peak}). \quad (19)$$

Note that the thermal attenuation coefficient is the ratio between the temperature at peak and the temperature of injection. Thus, a small thermal attenuation coefficient implies a large attenuation of the thermal amplitude, while a high thermal attenuation coefficient implies a limited attenuation of the thermal amplitude. The analytical expressions of the thermal lag time and attenuation coefficient for each fracture geometry (parallel plate and channel) and different flow fields (linear and dipole flow field), derived from the analytical solution presented in the previous section, are provided with more details in Appendix A. The different configurations are illustrated in Figure 1.

The expressions of the thermal lag time and attenuation coefficient for a parallel plate fracture in a linear flow field (Figure 1a) are (Appendix A)

$$\tau_{th} = 0.16 \left( \frac{2\rho_m c_m}{\rho_w c_w} \right)^2 D_m \frac{t_a^2}{a^2} \quad (20)$$

and

$$d_{th} = \left( \frac{\rho_w c_w}{2\rho_m c_m} \right)^2 \frac{1}{D_m} \frac{a^2}{t_a^2}, \quad (21)$$

where  $D_m = \lambda_m / \rho_m c_m$  is the thermal diffusivity of rock matrix ( $\text{m}^2/\text{s}$ ),  $\lambda_m$  is the thermal conductivity of rock matrix ( $\text{W} \cdot \text{m}^{-1} \cdot \text{K}^{-1}$ ),  $t_a = La/Q$  is the advective transit time (s),  $L$  is the distance between injection and withdrawal (m), and  $l$  is the fracture width normal to flow (m; Figure 1).

For  $n$  parallel and independent channels in a linear flow field (Figure 1b), the thermal lag time and attenuation coefficient are (Appendix A):

$$\tau_{th} = 0.16 \left( \frac{2\rho_m c_m}{\rho_w c_w} \right)^2 D_m \frac{(nt_a)^2}{a^2} \quad (22)$$

and

$$d_{th} = 0.8 \left( \frac{\rho_w c_w}{2\rho_m c_m} \right)^3 \frac{1}{D_m^2} \frac{a^4}{(nt_a)^3}, \quad (23)$$

**Table 1**  
Thermal Parameters of Water and Granite Used in the Models

Parameter	Thermal conductivity $\lambda_m$ ( $W \cdot m^{-1} \cdot K^{-1}$ )	Specific heat $c_m$ ( $J \cdot kg^{-1} \cdot K^{-1}$ )	Density $\rho_m$ ( $kg/m^3$ )
Water	0.59	4,200	1,000
Granite	3	740	2,470

Note. Incropera and DeWitt (1996) and Klepikova et al. (2016).

where  $t_a = \pi a^2 L / Q$  is the advective transit time (s). Note that in the multi-channel model, we do not consider thermal interaction between channels as we consider infinite matrix. The proposed multichannel model is thus consistent when channels are sufficient far away to not thermally interact each other during the time of the experiment.

Finally, the expressions of  $\tau_{th}$  and  $d_{th}$  for a parallel plate fracture in a dipole flow field (Figure 1c) are

$$\tau_{th} = 0.25 \left( \frac{2\rho_m c_m}{\rho_w c_w} \right)^2 D_m \frac{t_a^2}{a^2} \quad (24)$$

and

$$d_{th} = 0.2 \left( \frac{\rho_w c_w}{2\rho_m c_m} \right)^2 \frac{1}{D_m} \frac{a^2}{t_a^2}, \quad (25)$$

where  $t_a = \pi L^2 a / (3Q)$  is the breakthrough time for direct flow along the line joining the injection and withdrawal points (s; Barker, 2010). Note that the expressions derived here (equations (20) to (25)) are different from those derived by Luhmann et al. (2015), who assumed a separation of spatial and temporal variables for a sinusoidal input. Here we derived general expressions based on a transfer function valid for any input.

We validated all above expressions from numerical simulations using COMSOL Multiphysics®. The numerical simulations were performed with the thermal parameters of granite and water provided by Klepikova et al. (2016) and Incropera and DeWitt (1996; Table 1), for different fracture apertures ranging between 2.8 and 10 cm and for thermal fracture-matrix Péclet numbers ( $Pe_m = uL/D_m$ ) ranging between  $2 \cdot 10^3$  and  $4 \cdot 10^4$ . The Courant number  $N$  was used as a convergence condition of the numerical simulations such as  $N = u \times \Delta x / \Delta t$  with  $\Delta x$  the mesh size (m) and  $\Delta t$  the time stepping (s). For the channel and plane geometries in a linear flow field, we checked the good agreement between the numerical simulations with the analytical model given above for Courant numbers between 0.5 and 1. For the dipole flow field case, the numerical simulations were in agreement with the analytical model for a Courant number of 60, which shows the good agreement between the analytical solutions and the numerical model, even for relatively large mesh sizes. Note that these numerical simulations take into account transverse and longitudinal conduction within the matrix while in analytical models, only conduction perpendicular to the fracture occurs. This shows that for the simulated conditions, longitudinal conduction does not play a significant role on thermal transport in the fracture.

Note that the expression of the thermal lag time is similar for the different geometries, while the expression of the thermal attenuation coefficient  $d_{th}$  depends on the geometry. The thermal attenuation coefficient for a parallel plate fracture is proportional to  $1/t_a^2$ , while for a channel the thermal attenuation coefficient is proportional to  $1/t_a^3$  (equations (21), (23), and (25)). As discussed in the following, this property may be used to identify thermal signatures of highly channelized flow in fractured media. Figure 2 displays  $d_{th}$  as a function of  $t_a$  for a parallel plate, channel and multichannels of equivalent radius and aperture. This figure allows to discriminate the effect of fracture geometry on thermal conduction from the effect of flow velocity. Thus, it illustrates that for a given advection time and aperture, the thermal amplitude is more attenuated in a channel than in a parallel plate fracture. The thermal amplitude also appears more attenuated for a dipole flow field compared to the case of a linear flow field. This implies that thermal exchanges within the matrix are more efficient in a channel than in a parallel plate fracture. This difference is due to the dimensionality of the heat flux, which is radial (i.e., 2-D) for a channel and perpendicular to the fracture plane (i.e., 1-D) for a fracture (Klepikova et al., 2016). In a multichannel, the thermal attenuation coefficient is more important than in a single-channel as the multichannel configuration has a higher surface of exchange than the single-channel geometry.

#### 2.4. Comparison With the Thermal Retardation Factor in Porous Media

The expressions of thermal lag time in fractured media derived above can be compared with the expression of thermal retardation in porous media (equation (1)). For fractured media, equations (20), (22), and (24) can be combined to deduce the equivalent retardation factors for thermal transport in a channel and plane fracture in a linear flow field ( $R_{Tl}$ ) and in a plane fracture in a dipole flow field ( $R_{Td}$ ) as

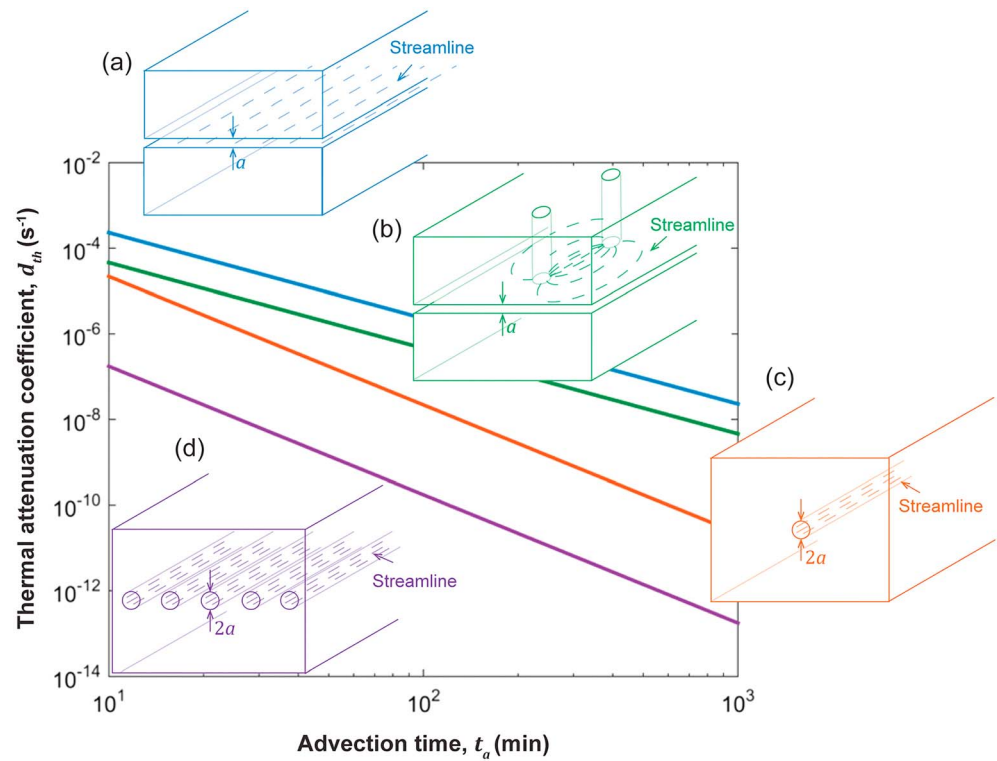


**Figure 2.** Thermal attenuation coefficient ( $d_{th}$ ) as a function of the advection time ( $t_a$ , arrival time of the solute breakthrough peak) for different flow fields and fracture geometries (equations (21), (23), and (25)): (a) a parallel plate fracture in a linear flow field (blue line), (b) a parallel plate fracture in a dipole flow field (green line), (c) a channel in a linear flow field (orange line), (d) five channels in a linear flow field (purple line). Radius and aperture are equal to  $a = 10$  mm.

$$R_{Tl} = 0.16 \frac{\lambda_m S}{Q \rho_w c_w a} \times \frac{\rho_m c_m}{\rho_w c_w} \quad \text{and} \quad R_{Td} = 0.08 \frac{\lambda_m S}{Q \rho_w c_w a} \times \frac{\rho_m c_m}{\rho_w c_w} \quad (26)$$

where  $S$  is the surface of exchange ( $m^2$ ). For a parallel plate fracture in a linear flow field,  $S = 2LH$ , for a channel in a linear flow field,  $S = 2\pi aL$ , and for a parallel plate fracture in a dipole flow field,  $S = 2\pi L^2$ . These expressions turn out to share some similarity with those known for porous media (equation (1)), where the volumetric ratio of fluid and solid is replaced by the ratio between the fracture/matrix thermal exchange factor (equal to  $\lambda_m S$ ) and the thermal advection factor (equal to  $Q \rho_w c_w a$ ). The  $\lambda_m S$  represents the capacity of rock matrix to exchange heat with the fluid, and  $Q \rho_w c_w a$  represents the advection processes in the fracture. The thermal retardation factor increases when increasing the surface of exchange between the fluid and the rock or the thermal conductivity or when reducing the flow rate or the fracture aperture. Note that contrary to thermal transport in porous media, instantaneous local equilibrium between the rock and the fluid cannot be assumed for fractured media. Hence, the expressions derived above for thermal lag time and attenuation coefficient cannot be used in the same way as for porous media. In the following, we show that they provide a new framework for interpreting field data and compare thermal tracer tests with solute tracer tests.

### 3. Field Setting and Experimental Setup

Our experimental setup consists of creating a single-well tracer test in a perfect dipole flow field, where hot water is injected in a chamber isolated by a double straddle packer, while water is pumped above in the same borehole. Hydraulic tests in vertical configuration have been implemented as vertical dipole flow tests to characterize the vertical hydraulic heterogeneity of a porous aquifer (Kabala, 1993; Zlotnik & Ledder, 1996; Zlotnik & Zurbuchen, 1998). A tracer test with a pulse input in such a dipole flow field can be performed to extract other properties such as dispersivity, anisotropy ratio, and dynamic volume (Chen et al., 2011;

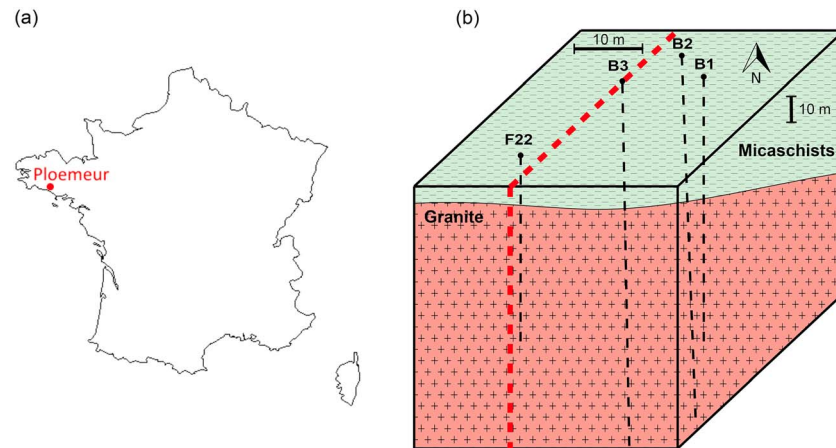


**Figure 3.** Location and geological diagram of the experimental site. (a) Map of France with the location of the Ploemeur town. (b) Geological block diagram of Stang er Brune experimental site with the locations of the different boreholes. The experiments were performed in the B3 borehole.

Sutton et al., 2000). The possibility to choose the size of the chamber and the distance between injection and withdrawal leads to reduce transfer times. Few vertical tracer tests using helium as a tracer have been performed previously at the experimental site of Stang er Brune (France), and in the same single-well dipole configuration (Chatton et al., 2017), showing the good connectivity of two permeable fractures crossing the same borehole at different depths. This setup can be compared to classical cross-borehole tests, except that only one borehole is instrumented.

### 3.1. Site Study

The experimental site of Stang er Brune is part of the fracture crystalline aquifer of Ploemeur (<http://hplus.ore.fr/en/ploemeur>). This aquifer is used for water supply since 1991 and monitored as a hydrological observatory to study hydraulic and transport properties of fractured media (H+ network of experimental sites; Le Borgne et al., 2006; Ruelleu et al., 2010). The experimental site is located near the outcrop of a contact zone between mica-schist and granite, which dips toward the north. Three open boreholes cross this contact zone at about 40 m as illustrated in Figure 3. A series of experiments have been performed at this site in the last 10 years, including flowmeter logging and straddle packer tests, to identify the permeable and well-connected fractures between boreholes (Le Borgne et al., 2007). Several tracer tests in dipole, convergent, and push pull configurations were performed to characterize the fracture network geometry and transport properties (Dorn et al., 2012; Kang et al., 2015; Klepikova et al., 2016). This site was also used to develop new hydrogeophysical methods for imaging flow and transport properties (Read et al., 2013; Schuite et al., 2017; Shakas et al., 2016).

The tracer tests were achieved in borehole B3 between fractures B3-1 and B3-2 located respectively around 36 and 45 m (Figure 4b). Hydraulic head measurements and previous solute tracer tests showed that these two fractures are hydraulically connected in the vicinity of the well. In particular, solute tracers can be transported from one fracture to the other in less than an hour for a pumping rate of  $2 \text{ m}^3/\text{hr}$  (Chatton et al., 2017). According to optical and acoustic imaging borehole logs and caliper data, B3-1 corresponds to a fractured zone located between 33.6- and 37.2-m deep (Figures 4a, 4d, 4e). Two subvertical parallel fractures have been identified from optical log around this depth. Fracture B3-2 is located at a depth of 44.9 m (Figures 4d and 4e). This fracture is well identified both from caliper data and flowmeter data (Figures 4a and 4b). Note that the flow decrease in front of B3-1 (Figure 4b) is due to the increase of borehole diameter at fracture zone depth. B3-1 is also well identified from ambient heat-pulse flowmeter data (Le Borgne et al., 2007) or borehole temperature logs (Figure 4c) which both reveal natural upward borehole flow toward B3-1, in agreement with the fact that the site is located in a groundwater upwelling area (Klepikova et al., 2014). However, it is not detected from impeller data (Figure 4b), since the hydraulic head in B3-1 in pumping condition is probably close to the borehole head. The fact that the temperature is relatively constant at depths greater than 33.6 m compared to the estimated natural geothermal gradient of the site (about  $16 \text{ }^\circ\text{C}/100 \text{ m}$ ) is the consequence of an upward flow of water, lower than  $2 \text{ L}/\text{min}$ , coming from deeper fractures toward B3-1, having a

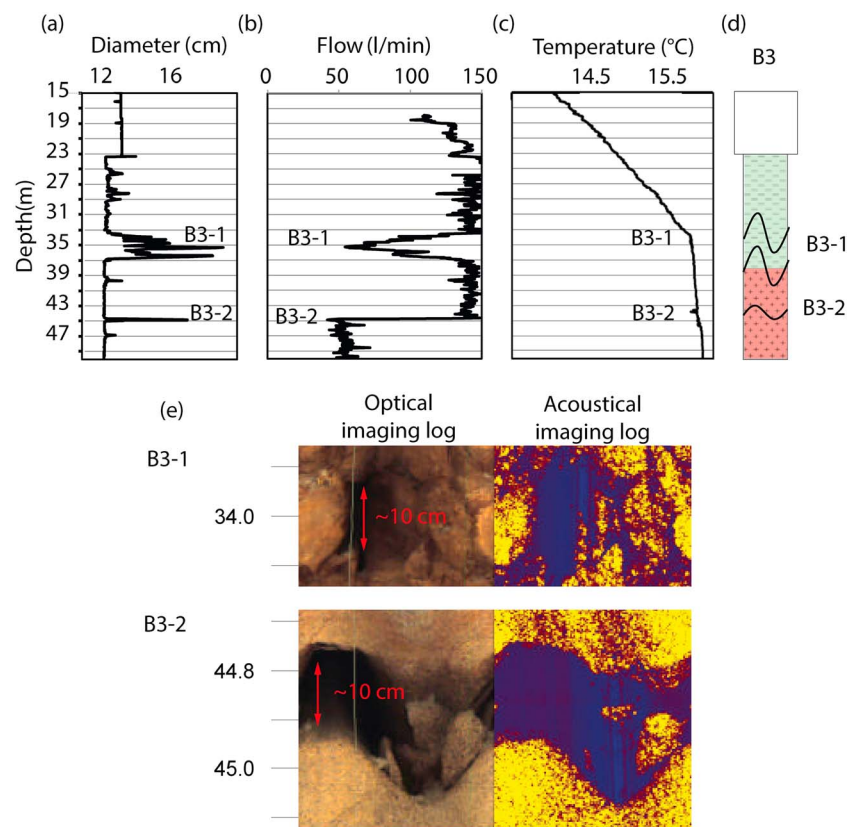


**Figure 4.** B3 logging data with (a) caliper log; (b) flow log measured with an impeller flowmeter while pumping at 140 L/min in the upper cased part of the well; (c) temperature log under ambient conditions; (d) geological log with fracture traces derived from optical and acoustic logs, where only the main fractures are represented; and (e) optical and acoustical imaging logs around the upper part of B3-1 and at B3-2 depth.

higher hydraulic head (Klepikova, 2013; Klepikova et al., 2011, 2014). Note also that the transmissivity of B3-1 ( $7.0 \times 10^{-4} \text{ m}^2/\text{s}$ ) is much lower than the transmissivity of B3-2 ( $2.4 \times 10^{-3} \text{ m}^2/\text{s}$ ; Le Borgne et al., 2007).

### 3.2. Experimental Set up

We performed three solute and four thermal tracer tests in a single-well configuration. Figure 5a displays a conceptual sketch of the single-well thermal tracer test, and Table 2 presents the experimental setup of the four tests. In this study, we present the results of the thermal tracer test IV (Table 2) achieved with a pulse input (56 °C during 13 min) in a dipole flow field with almost similar injection (15.6 L/min) and pumping rates (15 L/min). To estimate thermal lag time and attenuation coefficient, we compare the resulting thermal breakthrough to a solute breakthrough curve measured from a pulse injection of amino G acid (AGA; 0.07 g/L during 5.7 min) under a dipole configuration with comparable flow rates (injection rate of 16.5 L/min and pumping rate of 22 L/min). Since the pumped water is stored in a water tank before being reinjected between the packers, recirculation of thermal and solute tracers partly occurred during the experiment. We took this into account in the interpretation and modeling of the measured breakthrough curves.

For the tracer tests, the center of the chamber of the double straddle packer was installed at the depth of B3-2 fracture (44.9 m). The pressure was monitored above, in, and below the double-straddle packer to check that the packers well isolate the fractures in the borehole and to make sure steady-state flow conditions during the experiment. Above the packers, the water level was monitored at 10-s interval with a STS DL/N Series 70 data logger localized at 10-m depth. Pressure in and below the packers were monitored at 10-s interval using GE sensing PTX 1830 pressure transducers. The flow rate of water injection was monitored by a Liquiview FLM21-1 vortex flowmeter which measured continuously. Between the two packers, the

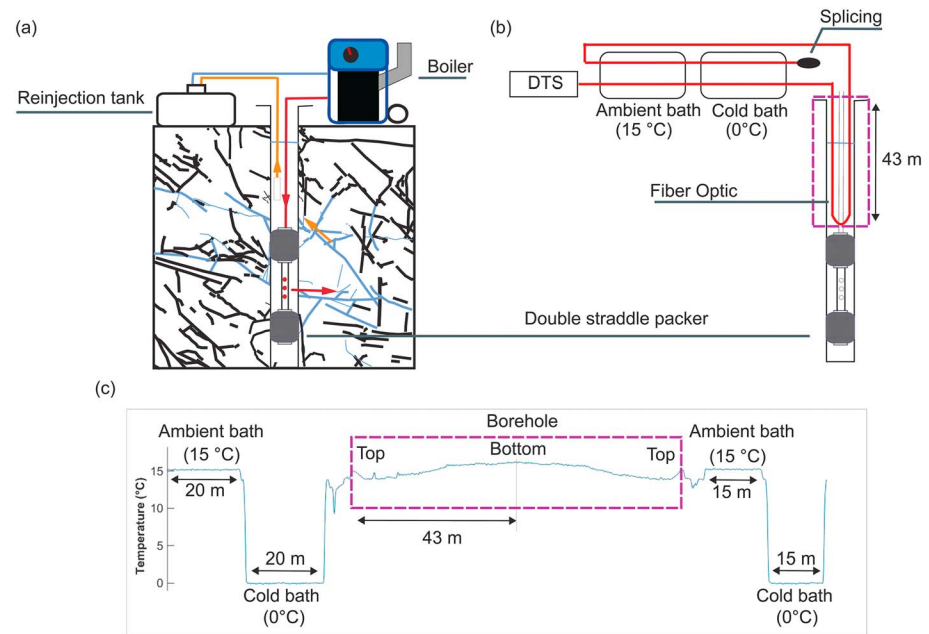


**Figure 5.** (a) Conceptual scheme of the experiment. (b) Calibration setup of the fiber-optic distributed temperature sensing (FO-DTS). The fiber optic cable is connected to the DTS unit, and then passes through both calibration bath before entering the borehole, down to the top of the straddle packer from which it goes out of the borehole before passing through each calibration baths a second time. (c) Example of fiber-optic distributed temperature measurements along the whole cable length.

injection temperature was monitored by a PT 100 temperature sensor. Amino G acid (AGA) tracer concentration was measured at 34-m depth using a borehole fluorimeter (Albillia GGUN-FL24). For each thermal tracer test, water was heated up to 60 °C with a boiler (DH 6 Swingtec). Heated water was injected using a VP Swingtec pump within the double straddle packer chamber. A rubber sleeve attached all along the injection tube was installed to limit heat losses. During the heat injection, the difference between the heating temperature of the boiler and the nearly constant temperature measured by the PT 100 sensor between the packers was about 3 °C, showing that there were only minor heat losses from the injection tube in the water column.

To localize and quantify the thermal breakthrough, a fiber-optic distributed temperature sensing (FO-DTS) was installed in the upper part of the borehole from the surface to the top of the double straddle packer at 43 m (Figure 5b) (Read et al., 2013). DTS monitoring was achieved using an Ultima S DTS units (SILIXA manufacturer), which allows a spatial sampling of 12.5 cm with a spatial resolution of about 29 cm. The sampling

**Table 2**  
*Experimental Setup of the Four Thermal Tracer Tests*

Tracer test	I	II	III	IV
Hydraulic configuration	Convergent dipole	Convergent dipole	Perfect dipole	Perfect dipole
Type of heat injection	Continuous injection	Continuous injection	Continuous injection	Pulse injection
Heat injection rate	16.2 L/min	16.7 L/min	16 L/min	15.6 L/min
Solute injection rate	4 L/min	10 L/min	10 L/min	
Pumping rate	125 L/min	90 L/min	22 L/min	15 L/min
Injection temperature	57.1 °C	55.9 °C	56.7 °C	56 °C
Injected mass of solute	1.32 g	1.39 g	1.32 g	
Duration of heat injection	4h50	2h10	4h02	13 min
Duration of solute injection	5 min 40	3 min	2 min	
Duration of heat recovery	15h14	13h10	17h24	

time was set to 1 min to reach a temperature resolution of 0.08 °C (see section 3.3). The fiber optic cable was led down in the borehole back and forth. Four coiled sections of cable were placed before and after entering in the borehole in two calibration baths respectively filled with water at ambient temperature (15 °C) and wetted ice (0 °C; Figures 5b and 5c). Accurate temperature sensors (RBR solo T temperature sensors with 0.002 °C accuracy) were installed in each bath to calibrate the FO-DTS. Three reference temperatures corresponding to three coiled sections located before the splicing were used for the calibration, two in the cold bath and one in the ambient bath. At 35 and 38 m two additional RBR solo T temperature sensors were installed to check the accuracy and the good calibration of the signal measured with FO-DTS.

### 3.3. Data Processing

RBR solo temperature probes in the two calibration baths were used to convert the laser backscattered signal measured by the FO-DTS unit to temperature using the post processing single ended calibration procedure proposed by Hausner et al. (2011). A temperature resolution (temporal mean of temperature variability along the fiber optic in calibration baths) of 0.08 °C was obtained, which is satisfactory given that heat recovery lead to a temperature increase of a few degrees Celsius. At 35 and 38 m, a mean absolute error of 0.13 °C was observed when comparing with downhole RBR solo T. This relative error may be attributed to the spatial temperature variability in the borehole and to the uncertainty in the exact depth of the temperature probes, which makes the comparison slightly uncertain. Nevertheless, FO-DTS provided very good and accurate estimates of temperature all along the borehole.

### 3.4. Thermal and Solute Analytical Models

We use the analytical expressions developed in section 2 to interpret the lag time and attenuation of thermal breakthrough curves with respect to solute breakthrough curves and infer information about flow topology in the fractures carrying the tracer. Furthermore, in order to model jointly the full thermal and solute breakthrough curve, we use transport models that considers solute and thermal dispersion in the fracture.

For modeling the full solute breakthrough curves under the assumption of parallel plate fracture in a dipole flow field, we use the Welty and Gelhar (1994) analytical solution (Constales et al., 2003; Sutton et al., 2000). This model solves the transient advection-dispersion equation along each streamline of a dipole flow field considering only longitudinal dispersion and neglecting molecular diffusion. The parameters are  $a$ , the fracture aperture, and  $\alpha$ , the longitudinal dispersivity. To simulate solute and heat transport under the assumption of channeled flow, we used the analytical solution developed by Becker and Shapiro (2000) in Laplace space. To adapt this model to the channel geometry, we replace, in equation (5) of Becker and Shapiro (2000), the memory function of a parallel plate fracture (equation (A3) in Appendix A), by the memory function of a channel (equation (A12) in Appendix A). The solution in Laplace space thus becomes

$$\bar{h}(p) = e^{\frac{L}{2a}} \left( 1 - \sqrt{1 + 4pt_0^2 \left( 1 + \sigma \frac{2}{\sqrt{p\tau}} \frac{K_1(\sqrt{p\tau})}{K_0(\sqrt{p\tau})} \right)} \right) \quad (27)$$

where  $t_r = a^2/D_m$  is the time for heat transfer in the matrix through a distance equal to the fracture aperture ( $s$ ) and  $K_i(z)$  is the modified Bessel function of the second kind (Abramowitz & Stegun, 1972). To simulate recirculation, we convolve the unit response to an instantaneous source obtained from analytical models (transfer function), with the recirculated concentration or temperature.

Note that in contrast to common dipole tests, the dipole tracer test is not achieved here between two boreholes but in a single borehole. In both configurations (cross borehole and single well), the flow field may be assumed to be composed of arc of circle streamlines with different radii intersecting the injection and the withdrawal area. The flux of water is split between a finite number of stream tubes with equal volumetric flow rates (Barker, 2010; Novakowski et al., 2004; Sutton et al., 2000; Welty & Gelhar, 1994). For simplification, we assume here that a perfect dipole single-well tracer test in a fracture can be simulated through models developed for perfect dipole cross-boreholes tracer tests. Uncertainties related to this assumption for a simplified fracture model should be, in any case, smaller than the uncertainties related to the complexity of the fracture network as either in cross-borehole or single-well configurations, the flow paths remain unknown and far from pure dipole flow field. Also, modeling the complexity of fracture network is one of the main difficulties when dealing with flow and transport in fractured rocks.

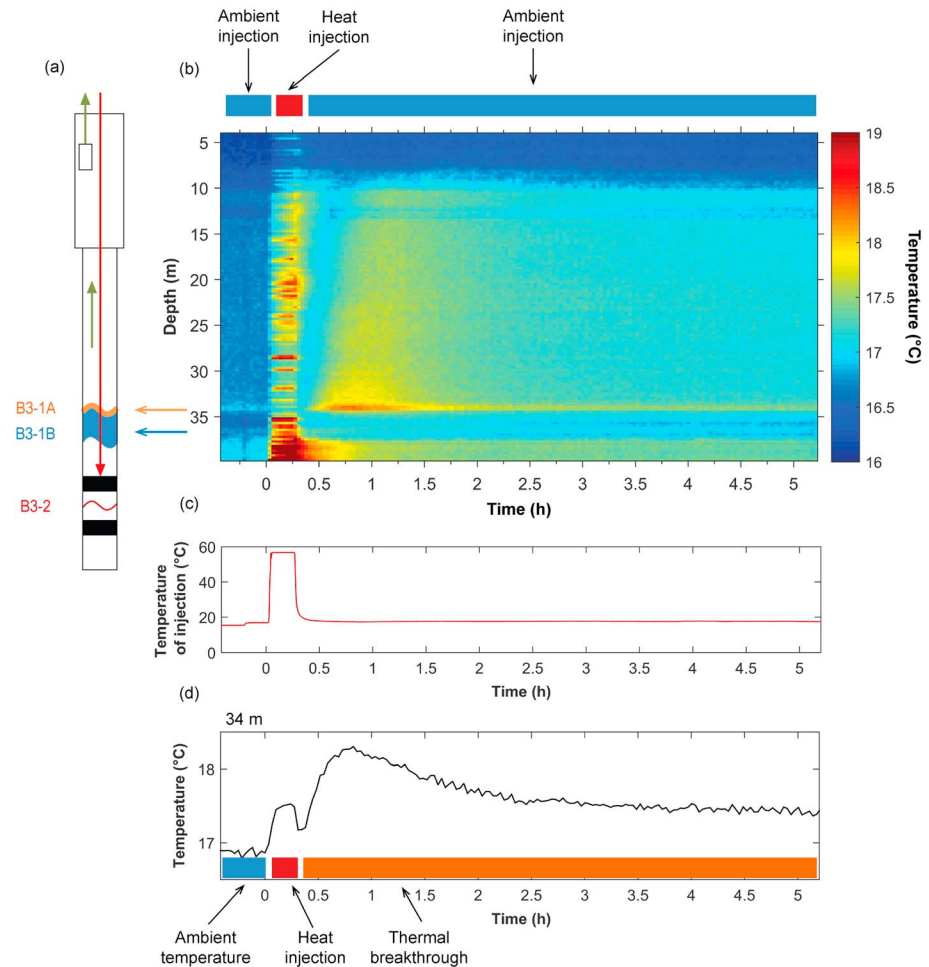


**Figure 6.** (a) B3 borehole scheme with the position of the injection fracture B3-2 (in red) and the hot inflow B3-1A (in orange) and cold inflow B3-1B (in blue) interpreted from (b) the measured temperature with the fiber-optic distributed temperature sensing (FO-DTS) during the perfect dipole experiment, where the x axis represents the time during the experiment, and the y axis corresponds to the depth in the borehole. (c) Temperature of injection measured in the injection chamber at B3-2 depth and (d) thermal breakthrough measured with the FO-DTS at hot inflow B3-1A (34 m).

## 4. Results

### 4.1. Temperature Breakthrough

Figure 6 displays the temperature measurement obtained with FO-DTS during the thermal tracer test above the straddle packer all along the injection tube in the water column. During the experiment, steady-state hydraulic conditions were maintained with negligible pressure variations neither in the injection chamber nor in the upper part of the borehole. The temperature in the injection zone was at ambient water temperature for both the beginning and the end of the experiment and reached 56 °C during heat injection (Figure 6c).

Before heat injection, the background temperature is roughly constant around 16.7 °C (Figure 6b). Note that the observed slight spatial variability of the ambient temperature is due to some small amount of heat remaining in fractures from previous thermal tracer tests. This background noise varies very slowly during the experiments and does not affect the results. During the 13 min heat injection, the temperature increases in the entire water column. Several hot stripes can be observed between 10 and 37.5 m with a warmer zone below 37.5 m. These temperature variations are due to thermal losses along the injection tube, which heat locally the water column by conduction. The stripes are located at the junctions between the sleeves, which isolate the injection tube. The larger temperature variations below 37.5 m occur in front of the steel tube of the packer, which has a much greater thermal conductivity.

Directly after the end of the heat injection, temperature decreases rapidly in most part of the water column due to the injection of ambient water in the injection tube and pumping of water at ambient temperature (Figure 6b). Pumping ensures renewal of water at ambient temperature, leading to the decrease of temperature along the borehole. Below 37.5 m, the temperature remains relatively high, which suggests the absence of flow in this zone. Directly, after the end of heat injection, an increase of temperature is observed between 33.6 and 34.5 m. The temperature of this hot spot increases up to 18.3 °C during 35 min before decreasing with time until the end of the experiment. As we shall see, this temperature increase corresponds to the breakthrough curve of the thermal tracer test, which is displayed in Figure 6d. Above 34 m, temperature also increases but to a lesser extent and with a delay that increases toward surface. Between 34.5 and 37.5 m, water temperature remains close to the ambient temperature as soon as heat injection stops. As we shall see in the next section, this near ambient temperature can be explained only by the presence of an ambient water inflow that decreases temperature sharply by advection. The lack of increase in temperature in this area also suggests that heat transfer from B3-2 to this zone is negligible during observation. At depth greater than 37.5 m, temperature decreases very slowly from 19 to 17.5 °C, which suggests the presence of immobile water where temperature decreases only by conduction.

These observations indicate the presence of the main inflow zone between 33.6 and 37.5 m, just above the no flow area. This 33.6 to 37.5 m area corresponds to the permeable fracture zone identified with caliper, flowmeter, and temperature profiles described in section 2. The DTS profile shows that the inflow is composed by water at ambient temperature between 34.5 and 37.5 m and by hot water between 33.6 and 34.5 m. The hot inflow corresponds to fast advection of heat from the B3-2 fracture and can be associated to thermal tracer breakthrough, while the cold inflow corresponds to another pathway. The relatively low temperature recovery suggests that this second pathway may be either disconnected from B3-2 or characterized by a large-temperature attenuation. In any case, this implies that at least two independent paths provide water to B3-1. In the following, we will make the distinction between the fracture zone located between 33.6 and 34.5 m, called B3-1A, and the fracture zone located between 34.5 and 37.5, called B3-1B. Above B3-1 fracture, cold and heat inflows are mixed and advected in the borehole by pumping at 10-m depth. Hence, the thermal tracer appears attenuated with a delay along the borehole. The delay is proportional to the flow velocity and the pumping rate, while the decay depends on the mixing rate.

The thermal breakthrough curve measured at 34 m (B3-1A), where thermal recovery is maximum, shows the different phases of the experiment (Figure 6d). Before the heating, temperature is equal to a background temperature of 16.9 °C. During heat injection and before thermal breakthrough, temperature increases slightly (0.5 °C above the initial temperature) due to heat losses along the injection tube close to the measurement zone. During the thermal breakthrough, the leading edge of the thermal tracer arrives 20 min after heat injection starts and the peak of the curve, which peaks at 1.3 °C above the initial temperature, arrives 50 min after injection starts. Then, temperature decreases slowly and is still 0.5 °C above the initial temperature at the end of the experiment. Note that the temperature measured above B3-1A is the result of the mixing of both inflows. To interpret the data and model the solute and thermal tracer breakthroughs, one needs to know how much flow comes from each inflow. In Appendix B, we present a simple procedure to estimate the contributions of B3-1A and B3-1B, which are respectively estimated to contribute 60% and 40% of the pumping flow rate. These flow estimates allow reconstructing the solute concentration breakthrough just before mixing in the borehole and to model both the solute and thermal breakthroughs. Note that here we assume the effect of the ambient upwelling flow on the thermal breakthrough to be negligible compared to the effect of the imposed flow rate as the ambient flow rate is much more lower than the pumping flow rate (see section 3.1).

#### 4.2. Solute Transport Modeling

The solute tracer breakthrough curve obtained under the same conditions as the thermal tracer test is displayed in Figure 7. Since the solute tracer was reinjected after dilution in the tank, a second peak of tracer can be observed. The concentration breakthrough is evolving toward a constant value for the late times, when the input concentration is diluted in the whole water volume. As discussed in the following, solute mass recovery was estimated from model fitting to be 60% for the entire breakthrough time (20 hr). This suggests that only the tracer coming from B3-1A was recovered, in agreement with flow estimate in the previous section and in Appendix B. Thus, we may consider that the concentration measured by the

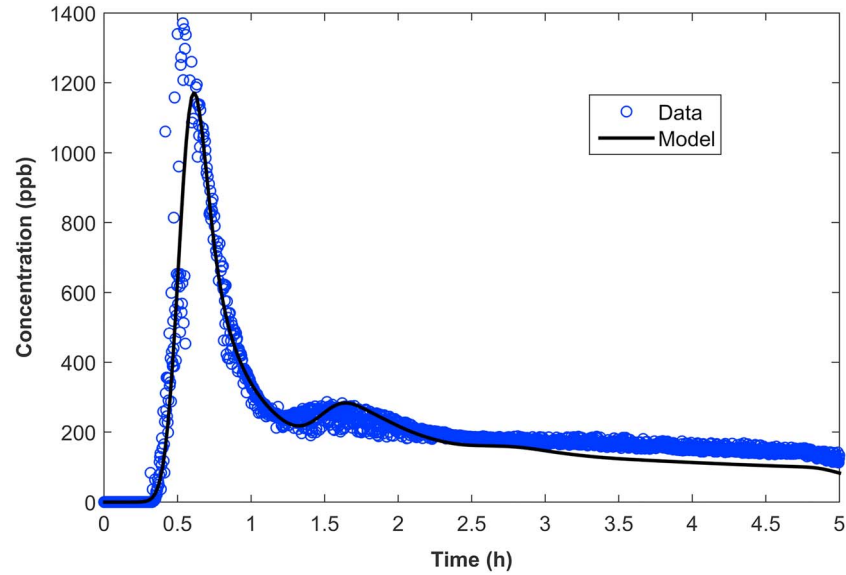


**Figure 7.** Amino G acid breakthrough coming from B3-1A calculated from fluorimeter measurements according to (27) (blue dots) and Welty and Gelhar (1994) model with recirculation (black line). The fitted parameters of the model are the fracture aperture,  $a = 3.3$  mm and the longitudinal dispersivity  $\alpha = 0.1$  m. The second peak is due to the recirculation of the tracer.

fluorimeter,  $C_{fluor}$ , corresponds to the concentration coming from B2-1A,  $C_{B3-1A}$ , diluted by the flow at B3-1B. Thus,  $C_{B3-1A}(t)$  can be calculated as

$$C_{B3-1A}(t) = \frac{C_{fluor}(t)}{0.6}. \quad (28)$$

The dipole flow field parallel plate model (see section 3.4) reproduces reasonably well the solute breakthrough curve as illustrated in Figure 7. The match to the data leads to a fracture aperture of 3.3 mm and a longitudinal dispersivity of 0.1 m, in agreement with other estimates at this site (Klepikova et al., 2016).

#### 4.3. Comparison Between Thermal and Solute Tracer Tests

In Figure 8, we compare the transfer functions of heat  $h(t)$  and solute  $h_s(t)$  obtained respectively from the breakthrough curves displayed in Figures 6d and 7. The  $h(t)$  and  $h_s(t)$  were calculated from (16) with  $Q = Q_i$ , corresponding to perfect dipole conditions as

$$h(t) = \frac{T_{B3-1A}(t)}{\Delta T_i \Delta t_i} \quad (29)$$

and

$$h_s(t) = \frac{C_{B3-1A}(t)}{C_i \Delta t_i^s}, \quad (30)$$

where  $Q_{B3-1A}$  and  $T_{B3-1A}$  are respectively the flow rate ( $m^3/s$ ) and the temperature (K) at B3-1A,  $C_i$  is the injected concentration of solute ( $g/m^3$ ), and  $\Delta t_i^s$  is the injection duration of solute (s). The thermal transfer function is strongly attenuated compared to the solute transfer function and the peak of heat arrives 14 min after the peak of solute, which corresponds to the thermal lag time. As the temperature of injection was continuously measured directly in front of B3-1B, the total injected heat was easily estimated, leading to a thermal recovery of about 15%. Characteristics of solute and thermal tracer tests are synthesized in Table 3.

The thermal fracture-matrix Péclet number was estimated equal to  $Pe_m = 3.3 \cdot 10^4$  from the thermal parameters measured from core samples (Table 1) and the advection time  $t_a$  obtained through the solute tracer test (see

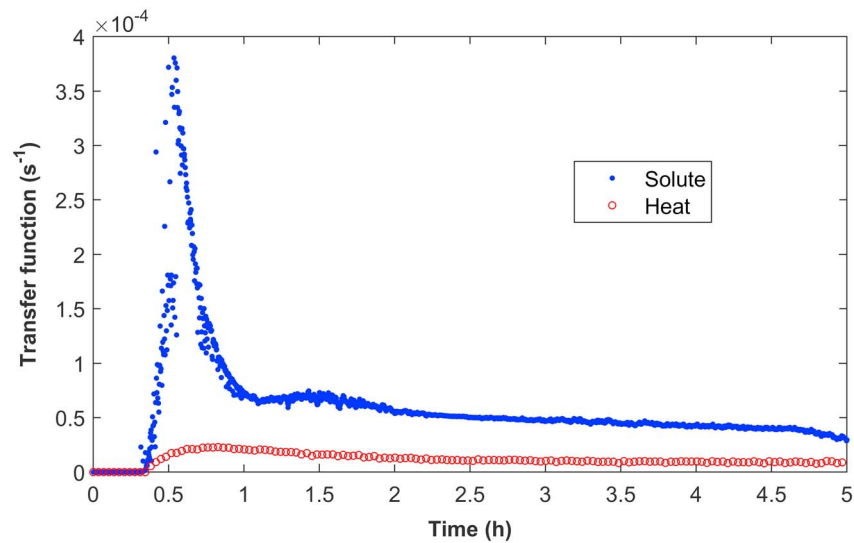


**Figure 8.** Comparison of the thermal transfer function (red circles) with the amino G acid solute transfer function (blue dots).

section 2.3). The Péclet number is therefore similar to the ones corresponding to the conditions used for the numerical simulations presented in section 2.3 when longitudinal conduction within the matrix does not influence thermal transport in the fracture. Thus, the theoretical framework developed in section 3.4, which considers only conduction perpendicular to the fracture is justified to interpret the thermal breakthrough. From equation (24) and (25), the expected thermal lag time and attenuation coefficient that would be expected for a dipole flow field in a parallel plate fracture can be estimated. For this, we take the thermal parameters measured from core samples (Table 1) and the advection time  $t_a$  and aperture  $a$  estimated from solute transport modeling. This leads to a thermal lag time of 28 hr and a thermal attenuation coefficient of  $5 \times 10^{-7} \text{ s}^{-1}$ . These values are clearly inconsistent with the thermal lag time and attenuation coefficient observed in Figure 8 (Table 3). Thus, this invalidates the assumption of a parallel plate fracture of homogeneous aperture for modeling both solute and thermal transport. This discrepancy is likely due to flow channeling, which leads to the reduction of thermal exchanges between fluid and rock in flow paths where fracture aperture is higher, and to the decrease of the thermal lag time and attenuation coefficient compared to a parallel plate fracture. Note that the first arrival times of heat and solute are quasi identical, which indicates that the first part of the thermal plume is mainly impacted by advection and does not have time to diffuse in the matrix certainly due to flow channeling. In the following, we explore the joint modeling of the thermal and solute breakthrough curves considering a channel geometry.

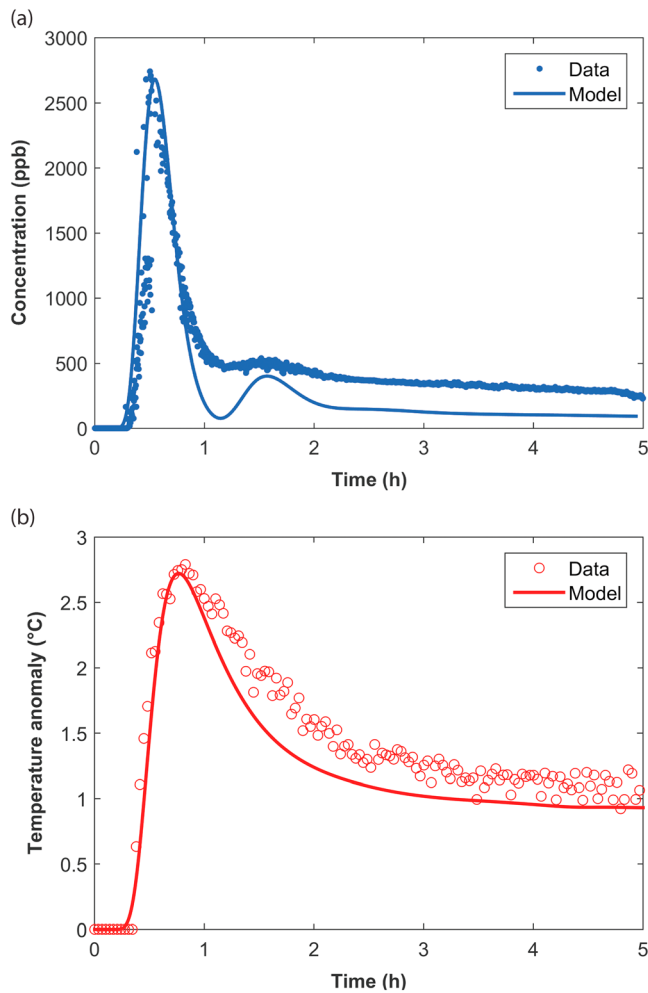
#### 4.4. Modeling Thermal and Solute Transport in a Channel

Figure 9 displays thermal and solute breakthroughs interpreted with a channel transport model (see section 3.4). The simulation matches reasonably well the first arrival time, the peak, and the amplitude for both thermal and solute breakthrough curves. The best match to both solute and thermal data was obtained for one single channel contributing to 30% of the total flow rate (50% of B3-1A flow rate).

Note that to calculate the solute breakthrough coming from the channel ( $C_{\text{channel}}$ ), we simply used the mixing equation  $C_{\text{channel}} = C_{\text{fluo}}/x_{\text{channel}}$ , where  $x_{\text{channel}}$  is the fraction of flow rate coming through the channel. The channel is characterized by the following parameters:  $a/L = 0.035$  and  $a = 3.8 \text{ cm}$ . The length of the corresponding channel may be determined from the model outputs such as  $L = x_{\text{channel}}Qt_a/\pi a^2$ . This leads to a length of about 30 m and a dispersivity of about 1 m. Such a length is larger than the distance between the withdrawal and the injection fractures (10.8 m).

**Table 3**  
Characteristics of Thermal and Solute Breakthroughs

Tracer	Heat	Solute (amino G acid)
Recovery ratio	15%	60%
Minimum transit time	20.7 min	16.8 min
Modal transit time	50 min	36 min
$d_{th}$ and $h_{peak}$	$2 \times 10^{-5}/s$	$3.8 \times 10^{-4}/s$



**Figure 9.** Modeling of the (a) amino G acid and (b) temperature breakthrough curves using the channel transport model (see section 3.4).

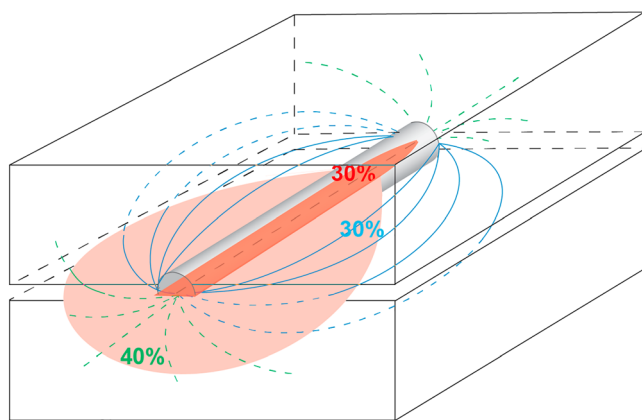


**Figure 10.** Conceptual scheme of the supposed fracture geometry with the different flow contributions during the perfect dipole single-well thermal and solute tracer tests. Pink corresponds to the fraction of thermal plume transported through the parallel plate fracture, which was not recovered (70%). Red corresponds to the fraction of thermal plume recovered through the channel (30%).

However, since the experiment was done between two fractures that intercept one each other in the neighborhood of the borehole, the real travel distance of tracers, or the tortuosity, may be significantly larger than the direct line joining the injection and withdrawal. Note that the peak of the thermal breakthrough curve may be well fitted for a slightly lower aperture (3.6 cm), even when dispersivity is not taken into account in the model. Considering the dispersivity in the model allows fitting the first arrival time and the tailing of the thermal breakthrough but does not have a significant impact on the aperture estimate. The dispersivity obtained from the channel model is 10 times higher than the one estimated from the solute transport modeling in a parallel plate fracture in a dipole flow field. This may be due to the fact that in the dipole model, dispersion is mainly due to the distribution of flow path lengths, while in the channel model, only longitudinal dispersivity along the channel influences dispersion. As in reality, flow lines within a large and tortuous channel may be quite complex, this may lead to a relatively high dispersivity that need to be taken into account in the model. The estimated channel diameter is also relatively large (7.6 cm) compared to other estimates from studies achieved in other boreholes at the same field site (1 cm; Klepikova et al., 2016). However, Figure 4e, which displays optical and acoustical imaging logs in front of B3-1A and B3-1, reveal the presence of a 10-cm hole, which is consistent with the aperture estimated from the channel model. The tailing of the solute breakthrough curve, which is not well captured by the model, despite the modeling of tracer recirculation (see section 3.4), suggests contributions from other flow paths that may result from dipole streamlines in the remaining of the fracture. The tailing of the thermal breakthrough curve is relatively well captured by the model, which suggests that the recovered heat was mainly transported through the identified channel.

Figure 10 summarizes the proposed conceptual geometry of the investigated fracture, deduced from the modeling of thermal and solute transport. This figure illustrates that 40% of the injected mass was not recovered during the time of the experiment and a half of the remaining 60% was transferred in a channel of 7.6-cm diameter. The other half may have been transported through a parallel plate fracture with an aperture of about 3.3 mm, following the streamlines of the dipole flow field. This flow partition model is consistent with the 15% of the injected heat recovered at B3-1A and the 60% of the total flow rate coming from B3-1A. Note however, that these estimations remain partly uncertain due to the number of model fitting parameters ( $\alpha/L$ ,  $a$ ,  $x_{\text{channel}}$ ) and the simplified assumed geometry for fractures. Nevertheless, despite those uncertainties, it is clear that (i) the pumped flow is splitted into at least two independent paths, (ii) a channel is required to model heat transport, and (iii) part of the solute is transported from the channel but also from other paths. In the following, we show that this interpretation is consistent with other thermal tracer tests performed between the same fracture zones but for different flow rates.

#### 4.5. Generalization to Other Thermal Tracer Tests

Since the sensitivity of the thermal attenuation coefficient to the advection time is different for the parallel plate fracture model and the channel model (equations (21), (23), and (25)), tracer tests performed under different flow velocities should discriminate the fracture flow geometry. Hence,

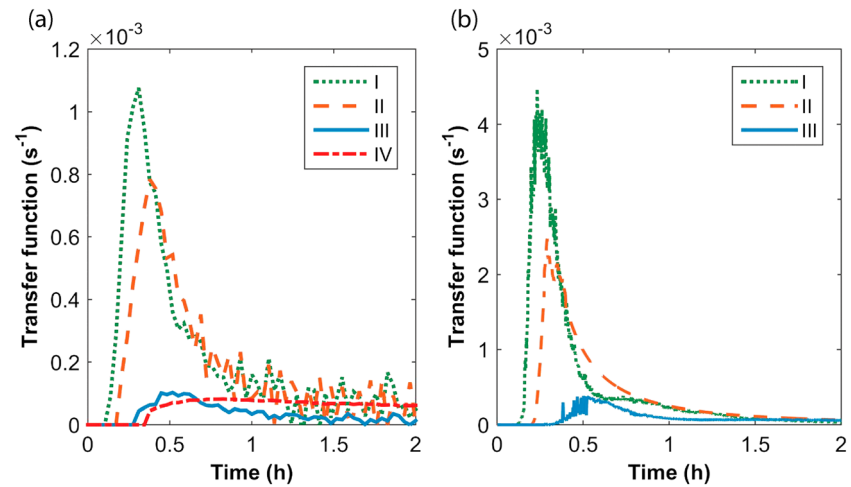


**Figure 11.** (a) Estimated thermal transfer functions in the channel assuming that the flow rate fraction through the channel is 30% (see section 4.4 and Figure 10) and (b) solute transfer functions of the whole tracer tests (see Table 2).

three additional single-well thermal and solute tracer tests achieved under continuous injection at different flow rates (i.e., different advective transit time  $t_a$ ) were used to evaluate the conceptual model defined above. One test was performed in dipole configuration with approximately the same flow rate as the tracer test interpreted previously. Two other tests were performed with a pumping rate larger than the

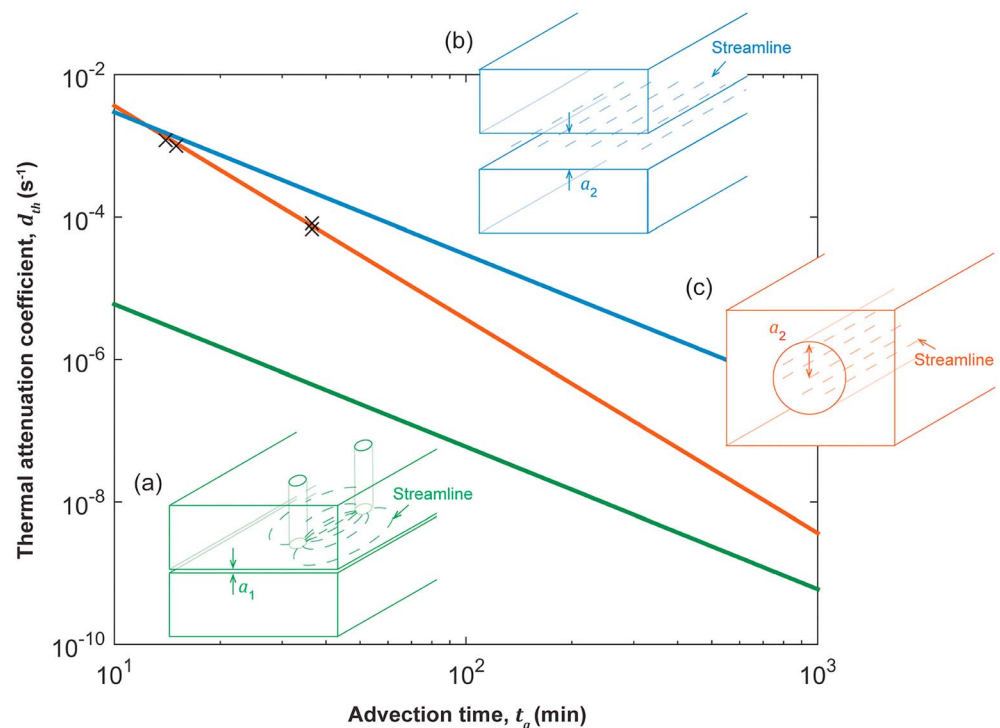


**Figure 12.** Thermal attenuation coefficient ( $d_{th}$ ) as a function of the advection time ( $t_a$ , arrival time of the solute breakthrough peak) for thermal tracer tests performed with different flow rates (cross markers). Comparison with the analytical expression of  $d_{th}$  as a function of  $t_a$  developed in section 2.3 for different fracture geometries and flow fields with (a) a parallel plate fracture in a dipole flow field of aperture  $a_1$ , the fracture aperture estimated from modeling of solute transport (green line); (b) a parallel plate fracture in a linear flow field of aperture  $a_2$  (blue line); and (c) a channel in a linear flow field of aperture  $a_2$  (orange line). The best match to the data was obtained for a channel of radius  $a_2 = 3.8$  cm which is about 10 times  $a_1$ .

injection rate (125 and 90 L/min for the pumping rates, while the injection rate was 16 L/min) (Table 2). According to equations (21), (23), and (25), the presence of a channel should be confirmed by representing the thermal attenuation coefficient  $d_{th}$  for the different tracer tests as a function of the advective transit time  $t_a$ . Equations (17) and (21) were used to determine the thermal transfer function  $h(t)$  (Figure 11) and then deduce  $d_{th}$  (Figure 12). Note that, similar to the previous thermal tracer test, the flow rate coming from B3-1A was calculated, thanks to equation (B1) in Appendix B, and the fraction of flow rate through the channel was assumed to be 30% (see section 4.4 and Figure 10). Thermal attenuation coefficient  $d_{th}$  is found to scale as  $1/t_a^3$ , in agreement with the scaling derived for the channel geometry (equation (23)), which supports the presence of a channel participating to the transport of heat. The scaling expected for parallel plate fracture of aperture equal to the one obtained with solute transport modeling in dipole configurations ( $a_1 = 3.3$  mm) largely overestimates the thermal amplitude attenuation. Furthermore, matching the thermal attenuation coefficient of the smallest travel time experiment by increasing the aperture in the parallel plate model in linear flow field leads to a significant underestimation of thermal amplitude attenuation for the other experiments, since the scaling with advection time is not consistent with the data. The channel model (equation (23)) is consistent with all three experiments using a radius  $a_2 = 3.6$  cm, in agreement with the previous estimate.

These findings show that flow channeling has two antagonist effects on thermal transport. On the one hand, by increasing locally the aperture, channeling leads to a smaller thermal amplitude attenuation than the parallel plate model of aperture  $a_1$  in dipole flow field (compare green and orange curves in Figure 12). On the other hand, for a given aperture and radius, the thermal amplitude attenuation is larger in the channel model as radial conduction is more efficient than linear conduction (compare blue and orange curves in Figure 12). For advection times corresponding to the presented experiments, the first effect appears to be predominant as thermal amplitude attenuation is lower for the channel of aperture  $a_2$  (orange curve in Figure 12) than for the parallel plate fracture of lower aperture  $a_1$  in dipole flow field (green curve in Figure 12), both matching the solute data as well. For large advection transit times ( $>30$  hr), the effect of the heat flux dimensionality is expected to prevail (as the orange curve will cross the green curve in Figure 12), implying that thermal amplitude attenuation will be eventually larger in the channel than in the parallel plate fracture in a dipole flow field.

## 5. Conclusion

We provide a new framework for interpreting joint solute and thermal tracer tests in fractured media, where analytical expressions for thermal lag time and attenuation coefficient allow discriminating different assumptions about fracture geometries and flow fields. Combining these analytical developments with the results of thermal and solute tracer tests, we uncover thermal signatures of flow channeling in fractured media, which are driven by two mechanisms that have antagonist effects on thermal transport. On the one hand, flow channeling in a rough fracture reduces thermal exchanges between the fluid and the rock due to flux convergence in the higher aperture zone and reduction of fluid residence time. On the other hand, flow channeling induces radial thermal conduction from channels to the matrix, which tends to increase thermal exchanges. The analytical expressions developed here allow to discriminate effectively the impact of both flow channeling effects on thermal transport during thermal tracer tests. For the considered thermal and solute tracer tests, we show that while solute breakthrough curve is the result of transport occurring in the whole fracture, recovered heat is mainly coming from a channel of higher aperture associated with small thermal lag time and attenuation coefficient.

The analytical expressions presented here may be a useful tool to predict thermal transport, during geothermal reservoir exploitation. In particular, if flow channeling occurs during the exploitation of a geothermal doublet, the thermal front may arrive either in advance or with a lag time at the withdrawal well compared to the prediction of a conventional parallel plate model, depending on the flow rate and the aperture of the channels, as quantified from our framework. These analytical expressions can thus predict whether flow channeling may reduce or extend the life duration of the geothermal reservoir, depending on channel properties and flow rates. Further analytical developments should consider multichannels and multifracture geometries taking into account thermal interactions between fractures or channels.

Finally, we highlight the interest of thermal tracer tests as a complement to solute tracer tests to infer fracture aperture and geometry. Thermal tracer tests are rarely achieved because of their difficulty to be implemented, although it is an essential in situ test to determine thermal storage capacity of fractured media. Because of their easier implementation, single-well thermal tracer tests can thus be an interesting alternative to cross-borehole thermal tracer tests. The use of FO-DTS for single-well thermal tracer tests is also an advantage compared to local temperature probe as it allows identifying, localizing, and quantifying heat inflows and heat mixing of the thermal tracer.

## Appendix A: Derivation of the Expressions of the Thermal Lag Time and Attenuation Coefficient for Different Fracture Geometries and Flow Fields

### A1. Linear Flow Field

#### A1.1 Parallel Plate Fracture

For a single fracture, imbedded in a matrix of infinite depth, the Green function is (Carslaw & Jaeger, 1959)

$$G(t, \eta) = \frac{\eta}{2\sqrt{\pi D_m t^3}} e^{-\frac{\eta^2}{4D_m t}}. \quad (A1)$$

In Laplace space, (A1) is (Carslaw & Jaeger, 1959)

$$\bar{G}(p, \eta) = e^{-\sqrt{\frac{p}{D_m}} \eta}. \quad (A2)$$

Thus, using (A2) in (11) for  $\sigma_m = 2/a$ , we obtain the memory function in Laplace space as

$$\bar{\varphi}(p) = \frac{2}{\sqrt{p t_r}}, \quad (A3)$$

where  $t_r = a^2/D_m$  is the time for heat transfer in the matrix through a distance equal to the fracture aperture ( $s$ ). Note that (A3) is the memory function presented by Haggerty et al. (2000) for diffusion in an infinite layer. Thus, using (14) and (15), the thermal transfer function in Laplace space is

$$\bar{h}(p) = e^{-p t_a \left(1 + \frac{2a}{\sqrt{p t_r}}\right)}. \quad (A4)$$

which can be written as

$$\bar{h}(p) = e^{-p t_a} e^{-\sqrt{\frac{(2t_a \sigma)^2}{t_r} p}} = e^{-p t_a} \bar{f}\left(\frac{(2t_a \sigma)^2}{t_r} p\right) \text{ where } \bar{f}(p') = e^{-\sqrt{p'}}. \quad (A5)$$

Thus,

$$h(t) = L^{-1}(\bar{h}(p)) = L^{-1}(e^{-p t_a}) * L^{-1}\left(\bar{f}\left(\frac{(2t_a \sigma)^2}{t_r} p\right)\right) \quad (A6)$$

and

$$h(t) = \delta(t - t_a) * \frac{t_r}{(2t_a \sigma)^2} f\left(\frac{t_r}{(2t_a \sigma)^2} t\right). \quad (A7)$$

We finally obtain

$$h(t) = L^{-1}(\bar{h}(p)) = \frac{t_r}{(2t_a \sigma)^2} f\left(\frac{t_r}{(2t_a \sigma)^2} (t - t_a)\right). \quad (A8)$$

We deduce from (A8), the thermal lag time ( $\tau_{th}$ ) and the thermal attenuation coefficient ( $d_{th}$ ) such as

$$\tau_{th} = t_{peak} - t_a = \frac{(2t_a\sigma)^2}{t_r} \tau_f \text{ and } d_{th} = \frac{t_r}{(2t_a\sigma)^2} f_{peak}, \quad (A9)$$

where  $\tau_f$  and  $f_{peak}$  are respectively the peak time and maximal value of the  $f$  function. After Laplace transform numerical inversion of  $F(p)$  using the Matlab function of Hollenbeck (1998), based on the algorithm of de Hoog (1982), we estimate  $\tau_f = 0.16$  and  $f_{peak} = 1$ . Thus, we finally obtain

$$\tau_{th} = 0.16 \frac{(2t_a\sigma)^2}{t_r} \text{ and } d_{th} = \frac{t_r}{(2t_a\sigma)^2}. \quad (A10)$$

### A1.2 Channel Fracture

For a single channel, imbedded in a matrix of infinite depth, the Green function in Laplace space is (Abramowitz & Stegun, 1972; Klepikova et al., 2016)

$$\bar{G}(p, \eta) = \frac{K_0\left(\sqrt{\frac{p}{D_m}} r\right)}{K_0\left(\sqrt{\frac{p}{D_m}} a\right)}, \quad (A11)$$

where  $K_i(z)$  is the modified Bessel function of the second kind (Abramowitz & Stegun, 1972). Thus, using (A11) in (11) for  $\sigma_m(\eta) = 2(a + \eta)/a^2$ , we obtain the memory function in Laplace space as

$$\bar{\varphi}(p) = \frac{2}{\sqrt{pt_r}} \left( \frac{K_1(\sqrt{pt_r})}{K_0(\sqrt{pt_r})} \right). \quad (A12)$$

Using (14) and (15), the thermal transfer function in Laplace space is

$$\bar{h}(p) = e^{-pt_a} \left( 1 + \frac{\sigma}{\sqrt{pt_r}} \frac{K_1(\sqrt{pt_r})}{K_0(\sqrt{pt_r})} \right), \quad (A13)$$

which can be written as

$$\bar{h}(p) = e^{-pt_a} e^{-\frac{2t_a\sigma}{t_r} \sqrt{pt_r} \frac{K_1(\sqrt{pt_r})}{K_0(\sqrt{pt_r})}} = e^{-pt_a} \bar{g}(pt_r) \text{ where } \bar{g}(p') = e^{-\frac{2t_a\sigma}{t_r} \sqrt{p'} \frac{K_1(\sqrt{p'})}{K_0(\sqrt{p'})}}. \quad (A14)$$

Using the same approach as (A6) to (A8), the inverse Laplace transform of  $\bar{h}(p)$  is

$$h(t) = L^{-1}(\bar{h}(p)) = \frac{1}{t_r} g\left(\frac{1}{t_r}(t - t_a)\right). \quad (A15)$$

The thermal lag time ( $\tau_{th}$ ) and the thermal attenuation coefficient ( $d_{th}$ ) are deduced from (A15) as

$$\tau_{th} = t_{peak} - t_a = t_r \tau_g \text{ and } d_{th} = \frac{1}{t_r} g(\tau_g) = \frac{1}{t_r} g_{peak}, \quad (A16)$$

where  $\tau_g$  and  $g_{peak}$  are respectively the peak time and the maximal value of the  $g$  function. After Laplace transform numerical inversion of  $\bar{g}(p)$ , we obtain  $\tau_g = 0.16 \left(\frac{2t_a}{t_r} \sigma\right)^2$  and  $g_{peak} = 0.8 \left(\frac{t_r}{2t_a\sigma}\right)^3$ . Thus, we obtain

$$\tau_{th} = 0.16 \frac{(2t_a\sigma)^2}{t_r} \text{ and } d_{th} = 0.8 \frac{t_r^2}{(2t_a\sigma)^3}. \quad (A17)$$

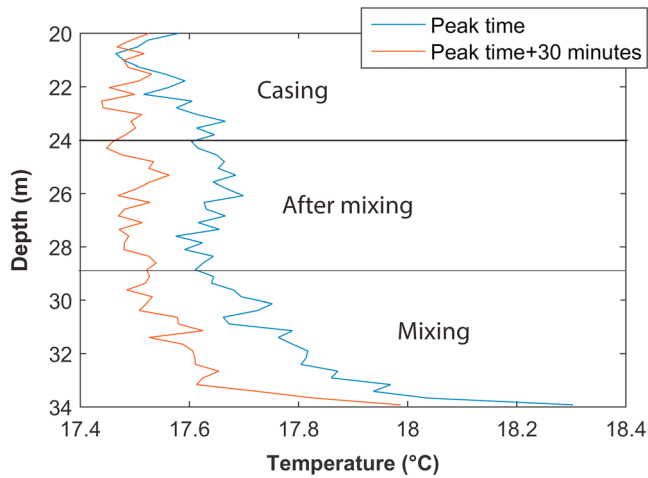


**Figure B1.** Reconstructed temperature profile in the borehole for two water volumes chosen at the peak time and 30 min after the peak time. To represent the data and reconstruct the temperature profile, a Lagrangian approach was used, which consists in considering the temperature evolution of the same water volume at different depths. This was achieved by taking into account the flow velocity in the borehole.

#### Acknowledgments

Funding was provided by the ANR project Stock en Socle (grant ANR-13-0009), the French network of hydrogeological observatories H+ (hplus.ore.fr/en) and the ANR project EQUIPEX CRITEX (grant ANR-11-EQPX-0011). Upon requesting a logging and a password at <http://hplus.ore.fr/en/database/acces-database>, the whole data set is available on the H+ website at [http://hplus.ore.fr/documents/requests/ploemeur/b3\\_FO\\_201509.csv.tgz](http://hplus.ore.fr/documents/requests/ploemeur/b3_FO_201509.csv.tgz) (FO-DTS), [http://hplus.ore.fr/documents/requests/ploemeur/b3\\_solute\\_201509.csv.tgz](http://hplus.ore.fr/documents/requests/ploemeur/b3_solute_201509.csv.tgz) (solute concentration), [http://hplus.ore.fr/documents/requests/ploemeur/b3\\_flowrate\\_201509.csv.tgz](http://hplus.ore.fr/documents/requests/ploemeur/b3_flowrate_201509.csv.tgz) (flow rate), [http://hplus.ore.fr/documents/requests/ploemeur/b3\\_Tinj\\_201509.csv.tgz](http://hplus.ore.fr/documents/requests/ploemeur/b3_Tinj_201509.csv.tgz) (injection temperature), and [http://hplus.ore.fr/documents/requests/ploemeur/b3\\_pressure\\_201509.csv.tgz](http://hplus.ore.fr/documents/requests/ploemeur/b3_pressure_201509.csv.tgz) (pressure). Travel grants from ECOS-Nord project N° C17U02 and UNESCO project IGCP636 are acknowledged. The authors wish to thank warmly Alain Dassargues and Serge Brouyère from the University of Liège for generously lending the portable water heater. We also would like to express our gratitude to Marco Dentz for his advices for the analytical developments and to René Lefebvre from INRS for his helpful comments and corrections. The authors finally thank the Associate Editor Olaf Cirpka who handled the manuscript and three anonymous reviewers for their thoughtful comments.

## A2. Dipole Flow Field

The response to an instantaneous source in a dipole flow field in a parallel fracture imbedded in a infinite rock matrix is (Barker, 2010)

$$h(t) = \frac{1}{\pi} \int_0^{\psi(t/t_a)} L^{-1} \left( e^{-pt_a\tau(\psi)} \left( 1 + \sigma \frac{\tau}{\sqrt{pr}} \right) \right) d\psi, \quad (A18)$$

where  $\psi$  is the angle of entry of the streamline into the withdrawal well and  $\tau$  in the dimensionless time  $t/t_a$ . Since the thermal lag time and the attenuation coefficient cannot be analytically determined from (A18), we resorted to numerical simulations. By running simulations over a range of parameters  $t_a$ ,  $\sigma$ , and  $t_r$ , we found similar expressions as for a linear flow field (A19) with a corrected prefactor as

$$\tau_{th} = 0.25 \frac{(2t_a\sigma)^2}{t_r} \text{ and } d_{th} = 0.2 \frac{t_r}{(2t_a\sigma)^2}. \quad (A19)$$

## Appendix B: Determination of the Flow Distribution in the Borehole Above the Packers

The temperature measured above B3-1A is the result of the mixing of both the cold and hot inflows. The FO-DTS temperature monitoring along the

borehole (Figure B1) shows that the mixing is complete at about 29 m, with very low temperature variations between this depth and 24 m, the bottom of casing. However, large-temperature variations are observed between 29 and 34 m. These fluctuations were interpreted as the result of the mixing between the cold inflow at B3-1B and the hot inflow from B3-1A measured at 34 m. The fraction of flow coming from B3-1A and B3-1B should be constant as steady-state hydraulic conditions were maintained during all the experiment. Thus, by assuming that the temperature of B3-1A was effectively measured at 34 m through FO-DTS before mixing, it is possible to estimate the fraction of flow coming from B3-1A from the mixing equation

$$Q_{B3-1A} = Q \frac{\tilde{T}_{mix} - \tilde{T}_{B3-1B}}{\tilde{T}_{B3-1A} - \tilde{T}_{B3-1B}}, \quad (B1)$$

where  $Q_{B3-1A}$  is the flow rate coming from B3-1A ( $m^3/s$ ),  $Q$  is the total pumping rate ( $m^3/s$ ),  $\tilde{T}_{mix}$  is the mixing temperature measured in the borehole between 24 and 29 m (K),  $\tilde{T}_{B3-1B}$  is the temperature measure in front of B3-1B(K), and  $\tilde{T}_{B3-1A}$  is the temperature measures in front of B3-1A(K). This leads to  $Q_{B3-1A} = 9.4$  L/min, which corresponds to approximately 60% of the total pumping rate. Thus, since the dipole flow field was theoretically closed (all injected water should be recovered at infinite time), we estimate that 60% of the injected heat was transported by B3-1A (but not necessarily recovered), while 40% was transported by B3-1B but was not detected during the time of the experiment. B3-2.

## References

- Abramowitz, M., & Stegun, I. (1972). *Handbook of mathematical functions with formulas, graphs and mathematical tables*. New-York: John Wiley.
- Anderson, M. P. (2005). Heat as a ground water tracer. *Ground Water*, 43(6), 951–968. <https://doi.org/10.1111/j.1745-6584.2005.00052.x>
- Axelsson, G., Flovenz, A. G., Hauksdottir, S., Hjartarson, A., & Liu, J. R. (2001). Analysis of tracer test data, and injection-induced cooling, in the Laugaland geothermal field, N-Iceland. *Geothermics*, 30(6), 697–725. [https://doi.org/10.1016/s0375-6505\(01\)00026-8](https://doi.org/10.1016/s0375-6505(01)00026-8)
- Banks, D. (2009). Thermogeological assessment of open-loop well-doublet schemes: A review and synthesis of analytical approaches. *Hydrogeology Journal*, 17(5), 1149–1155. <https://doi.org/10.1007/s10040-008-0427-6>
- Barker, J. A. (2010). Modelling doublets and double porosity. *Quarterly Journal of Engineering Geology and Hydrogeology*, 43(3), 259–268. <https://doi.org/10.1144/1470-9236/08-095>
- Becker, M. W., & Shapiro, A. M. (2000). Tracer transport in fractured crystalline rock: Evidence of nondiffusive breakthrough tailing. *Water Resources Research*, 36(7), 1677–1686. <https://doi.org/10.1029/2000wr900080>
- Bense, V. F., Read, T., Bour, O., Le Borgne, T., Coleman, T., Krause, S., et al. (2016). Distributed temperature sensing as a downhole tool in hydrogeology. *Water Resources Research*, 52, 9259–9273. <https://doi.org/10.1002/2016wr018869>

- Berkowitz, B. (2002). Characterizing flow and transport in fractured geological media: A review. *Advances in Water Resources*, 25(8–12), 861–884. [https://doi.org/10.1016/s0309-1708\(02\)00042-8](https://doi.org/10.1016/s0309-1708(02)00042-8)
- Bodvarsson, G. S., & Tsang, C. F. (1982). Injection and thermal breakthrough in fractured geothermal-reservoirs. *Journal of Geophysical Research*, 87(B2), 1031–1048. <https://doi.org/10.1029/JB087iB02p01031>
- Burns, E. R., Ingebritsen, S. E., Manga, M., & Williams, C. F. (2016). Evaluating geothermal and hydrogeologic controls on regional groundwater temperature distribution. *Water Resources Research*, 52, 1328–1344. <https://doi.org/10.1002/2015wr018204>
- Carrera, J., Sanchez-Vila, X., Benet, I., Medina, A., Galarza, G., & Guimera, J. (1998). On matrix diffusion: Formulations, solution methods and qualitative effects. *Hydrogeology Journal*, 6(1), 178–190. <https://doi.org/10.1007/s100400050143>
- Carslaw, H. S., & Jaeger, J. C. (1959). *Conduction of Heat in Solids*. Oxford: Science Publications.
- Chatton, E., Labasque, T., de La Bernardie, J., Guiheneuf, N., Bour, O., & Aquilina, L. (2017). Field continuous measurement of dissolved gases with a CF-MIMS: Applications to the physics and biogeochemistry of groundwater flow. *Environmental Science & Technology*, 51(2), 846–854. <https://doi.org/10.1021/acs.est.6b03706>
- Chen, J. S., Liu, C. W., Chan, Y. C., Ni, C. F., & Kao, K. K. (2011). Effect of transverse dispersion on solute transport in a vertical dipole flow test with a tracer. *Journal of Hydrology*, 402(3–4), 206–216. <https://doi.org/10.1016/j.jhydrol.2011.03.005>
- Cherubini, C., Pastore, N., Giasi, C. I., & Allegretti, N. M. (2017). Laboratory experimental investigation of heat transport in fractured media. *Nonlinear Processes in Geophysics*, 24(1), 23–42. <https://doi.org/10.5194/npg-24-23-2017>
- Constales, D., Kacur, J., & Malengier, B. (2003). A precise numerical scheme for contaminant transport in dual-well flow. *Water Resources Research*, 39(10), 1303. <https://doi.org/10.1029/2003wr002411>
- Curewitz, D., & Karson, J. A. (1997). Structural settings of hydrothermal outflow: Fracture permeability maintained by fault propagation and interaction. *Journal of Volcanology and Geothermal Research*, 79(3–4), 149–168. [https://doi.org/10.1016/s0377-0273\(97\)00027-9](https://doi.org/10.1016/s0377-0273(97)00027-9)
- de Hoog, F. R., Knight, J. H., & Stokes, A. N. (1982). An improved method for numerical inversion of Laplace transforms. *SIAM Journal on Scientific and Statistical Computing*, 3(3), 357–366. <https://doi.org/10.1137/0903022>
- de La Bernardie, J., de Dreuzy, J.-R., Bour, O., & Lesueur, H. (2019). Synthetic investigation of thermal storage capacities in crystalline bedrock through a regular fracture network as heat exchanger. *Geothermics*, 77, 130–138. <https://doi.org/10.1016/j.geothermics.2018.08.010>
- Dorn, C., Linde, N., Le Borgne, T., Bour, O., & Klepikova, M. (2012). Inferring transport characteristics in a fractured rock aquifer by combining single-hole ground-penetrating radar reflection monitoring and tracer test data. *Water Resources Research*, 48, W11521. <https://doi.org/10.1029/2011wr011739>
- Geiger, S., & Emmanuel, S. (2010). Non-Fourier thermal transport in fractured geological media. *Water Resources Research*, 46. <https://doi.org/10.1029/2009wr008671>, W07504.
- Gerard, A., Genter, A., Kohl, T., Lutz, P., Rose, P., & Rummel, F. (2006). The deep EGS (enhanced geothermal system) project at Soultz-sous-Forets (Alsace, France). *Geothermics*, 35(5–6), 473–483. <https://doi.org/10.1016/j.geothermics.2006.12.001>
- Gringarten, A. C., Witherspoon, P. A., & Ohnishi, Y. (1975). Theory of heat extraction from fractured hot dry rock. *Journal of Geophysical Research*, 80(8), 1120–1124. <https://doi.org/10.1029/JB080i008p01120>
- Guo, B., Fu, P. C., Hao, Y., Peters, C. A., & Carrigan, C. R. (2016). Thermal drawdown-induced flow channeling in a single fracture in EGS. *Geothermics*, 61, 46–62. <https://doi.org/10.1016/j.geothermics.2016.01.004>
- Haggerty, R., McKenna, S. A., & Meigs, L. C. (2000). On the late-time behavior of tracer test breakthrough curves. *Water Resources Research*, 36(12), 3467–3479. <https://doi.org/10.1029/2000wr900214>
- Haring, M. O., Schanz, U., Ladner, F., & Dyer, B. C. (2008). Characterisation of the Basel 1 enhanced geothermal system. *Geothermics*, 37(5), 469–495. <https://doi.org/10.1016/j.geothermics.2008.06.002>
- Hausner, M. B., Suarez, F., Glander, K. E., van de Giesen, N., Selker, J. S., & Tyler, S. W. (2011). Calibrating single-ended Fiber-optic Raman spectra distributed temperature sensing data. *Sensors*, 11(11), 10,859–10,879. <https://doi.org/10.3390/s111110859>
- Hawkins, A. J., Becker, M. W., & Tsoflias, G. P. (2017). Evaluation of inert tracers in a bedrock fracture using ground penetrating radar and thermal sensors. *Geothermics*, 67, 86–94. <https://doi.org/10.1016/j.geothermics.2017.01.006>
- Heuer, N., Kupper, T., & Windelberg, D. (1991). Mathematical-model of a hot dry rock system. *Geophysical Journal International*, 105(3), 659–664. <https://doi.org/10.1111/j.1365-246X.1991.tb00803.x>
- Hollenbeck, K. (1998). INVLAP.M: A matlab function for numerical inversion of Laplace transforms by the Hoog algorithm. Retrieved from <http://www.isva.dtu.dk/staff/karl/invlap.htm>
- Incropera, F. P., & DeWitt, D. P. (1996). *Fundamentals of heat and mass transfer* (fourth ed.). New York: John Wiley and Sons.
- Kabala, Z. J. (1993). The dipole flow test - a new single-borehole test for aquifer characterization. *Water Resources Research*, 29(1), 99–107. <https://doi.org/10.1029/92wr01820>
- Kang, P. K., Le Borgne, T., Dentz, M., Bour, O., & Juanes, R. (2015). Impact of velocity correlation and distribution on transport in fractured media: Field evidence and theoretical model. *Water Resources Research*, 51, 940–959. <https://doi.org/10.1002/2014wr015799>
- Kim, J., Lee, Y., Yoon, W. S., Jeon, J. S., Koo, M. H., & Keehm, Y. (2010). Numerical modeling of aquifer thermal energy storage system. *Energy*, 35(12), 4955–4965. <https://doi.org/10.1016/j.energy.2010.08.029>
- Klepikova, M. (2013). Imaging of fractured rock properties from flow and heat transport: field experiments and inverse modelling. (Doctoral dissertation). Rennes: Université de Rennes 1.
- Klepikova, M., Le Borgne, T., Bour, O., & Davy, P. (2011). A methodology for using borehole temperature-depth profiles under ambient, single and cross-borehole pumping conditions to estimate fracture hydraulic properties. *Journal of Hydrology*, 407, 145–152. <https://doi.org/10.1016/j.jhydrol.2011.07.018>
- Klepikova, M., Le Borgne, T., Bour, O., Dentz, M., Hochreutener, R., & Lavenant, N. (2016). Heat as a tracer for understanding transport processes in fractured media: Theory and field assessment from multiscale thermal push-pull tracer tests. *Water Resources Research*, 52, 5442–5457. <https://doi.org/10.1002/2016wr018789>
- Klepikova, M., Le Borgne, T., Bour, O., Gallagher, K., Hochreutener, R., & Lavenant, N. (2014). Passive temperature tomography experiments to characterize transmissivity and connectivity of preferential flow paths in fractured media. *Journal of Hydrology*, 512, 549–562. <https://doi.org/10.1016/j.jhydrol.2014.03.018>
- Lauwerier, H. A. (1955). The transport of heat in an oil layer caused by the injection of hot fluid. *Applied Scientific Research*, 5(2-3), 145–150. <https://doi.org/10.1007/BF03184614>
- Le Borgne, T., Bour, O., Paillet, F. L., & Caudal, J. P. (2006). Assessment of preferential flow path connectivity, and hydraulic properties at single-borehole and cross-borehole scales in a fractured aquifer. *Journal of Hydrology*, 328(1–2), 347–359. <https://doi.org/10.1016/j.jhydrol.2005.12.029>

- Le Borgne, T., Bour, O., Riley, M. S., Gouze, P., Pezard, P. A., Belghoul, A., et al. (2007). Comparison of alternative methodologies for identifying and characterizing preferential flow paths in heterogeneous aquifers. *Journal of Hydrology*, *345*(3–4), 134–148. <https://doi.org/10.1016/j.jhydro.2007.07.007>
- Luhmann, A. J., Covington, M., Myre, J., Perne, M., Jones, S. W., Alexander, E. C. Jr., & Saar, M. (2015). Thermal damping and retardation in karst conduits. *Hydrology and Earth System Sciences*, *19*, 137–157. <https://doi.org/10.5194/hess-19-137-2015>
- Malkovsky, V. I., & Magri, F. (2016). Thermal convection of temperature-dependent viscous fluids within three-dimensional faulted geothermal systems: Estimation from linear and numerical analyses. *Water Resources Research*, *52*, 2855–2867. <https://doi.org/10.1002/2015wr018001>
- Manga, M., & Kirchner, J. W. (2004). Interpreting the temperature of water at cold springs and the importance of gravitational potential energy. *Water Resources Research*, *40*, W05110. <https://doi.org/10.1029/2003wr002905>
- Menberg, K., Pfister, S., Blum, P., & Bayer, P. (2016). A matter of meters: State of the art in the life cycle assessment of enhanced geothermal systems. *Energy & Environmental Science*, *9*(9), 2720–2743. <https://doi.org/10.1039/c6ee01043a>
- Molson, J., Pehme, P. E., Cherry, J., & Parker, B. (2007). Numerical analysis of heat transport within fractured sedimentary rock: Implications for temperature probes. Paper presented at the NGWA/U.S. EPA Fractured Rock Conference: State of the Portland, Maine.
- Molson, J. W., Frind, E. O., & Palmer, C. D. (1992). Thermal-energy storage in an unconfined aquifer.2. Model development, validation, and application. *Water Resources Research*, *28*(10), 2857–2867. <https://doi.org/10.1029/92wr01472>
- Molz, F. J., Warman, J. C., & Jones, T. E. (1978). Aquifer storage of heated water.1. field experiment. *Ground Water*, *16*(4), 234–241. <https://doi.org/10.1111/j.1745-6584.1978.tb03230.x>
- Neuman, S. P. (2005). Trends, prospects and challenges in quantifying flow and transport through fractured rocks. *Hydrogeology Journal*, *13*(1), 124–147. <https://doi.org/10.1007/s10040-004-0397-2>
- Neuville, A., Toussaint, R., & Schmittbuhl, J. (2010). Hydrothermal coupling in a self-affine rough fracture. *Physical Review E*, *82*(3), 14. <https://doi.org/10.1016/j.crte.2009.03.006>
- Novakowski, K. S., Bickerton, G., & Lapcevic, P. (2004). Interpretation of injection-withdrawal tracer experiments conducted between two wells in a large single fracture. *Journal of Contaminant Hydrology*, *73*(1–4), 227–247. <https://doi.org/10.1016/j.jconhyd.2004.02.001>
- Olasolo, P., Juarez, M. C., Morales, M. P., D'Amico, S., & Liarte, I. A. (2016). Enhanced geothermal systems (EGS): A review. *Renewable & Sustainable Energy Reviews*, *56*, 133–144. <https://doi.org/10.1016/j.rser.2015.11.031>
- O'Sullivan, M. J., Pruess, K., & Lippmann, M. J. (2001). State of the art of geothermal reservoir simulation. *Geothermics*, *30*(4), 395–429. [https://doi.org/10.1016/s0375-6505\(01\)00005-0](https://doi.org/10.1016/s0375-6505(01)00005-0)
- Pasquier, P., Nguyen, A., Eppner, F., Marcotte, D., & Baudon, P. (2016). Standing column wells. In S. Rees (Ed.), *Advances in ground-source heat pump systems* (pp. 269–294). Duxford: Woodhead Publishing.
- Pastore, N., Cherubini, C., Rapti, D., & Giasi, C. I. (2018). Experimental study of forced convection heat transport in porous media. *Nonlinear Processes in Geophysics*, *25*(2), 279–290. <https://doi.org/10.5194/npg-25-279-2018>
- Person, M., Hofstra, A., Sweetkind, D., Stone, W., Cohen, D., Gable, C. W., & Banerjee, A. (2012). Analytical and numerical models of hydro-thermal fluid flow at fault intersections. *Geofluids*, *12*(4), 312–326. <https://doi.org/10.1111/gfl.12002>
- Read, T., Bour, O., Bense, V., Le Borgne, T., Goderniaux, P., Klepikova, M. V., et al. (2013). Characterizing groundwater flow and heat transport in fractured rock using fiber-optic distributed temperature sensing. *Geophysical Research Letters*, *40*, 2055–2059. <https://doi.org/10.1002/grl.50397>
- Rode, A., Liesch, T., & Goldscheider, N. (2015). Open-loop geothermal heating by combined extraction-injection one-well systems: A feasibility study. *Geothermics*, *56*, 110–118. <https://doi.org/10.1016/j.geothermics.2015.03.001>
- Ruelleu, S., Moreau, F., Bour, O., Gapais, D., & Martelet, G. (2010). Impact of gently dipping discontinuities on basement aquifer recharge: An example from Ploemeur (Brittany, France). *Journal of Applied Geophysics*, *70*(2), 161–168. <https://doi.org/10.1016/j.jappgeo.2009.12.007>
- Ruiz Martinez, A., Roubinet, D., & Tartakovsky, D. M. (2014). Analytical models of heat conduction in fractured rocks. *Journal of Geophysical Research: Solid Earth*, *119*, 83–98. <https://doi.org/10.1002/2012jb010016>
- Saar, M. O. (2011). Review: Geothermal heat as a tracer of large-scale groundwater flow and as a means to determine permeability fields. *Hydrogeology Journal*, *19*(1), 31–52. <https://doi.org/10.1007/s10040-010-0657-2>
- Sauty, J. P., Gringarten, A. C., Menjoz, A., & Landel, P. A. (1982). Sensible energy-storage in aquifers.1. Theoretical-study. *Water Resources Research*, *18*(2), 245–252. <https://doi.org/10.1029/WR018i002p00245>
- Schuite, J., Longuevergne, L., Bour, O., Guiheneuf, N., Becker, M. W., Cole, M., et al. (2017). Combining periodic hydraulic tests and surface tilt measurements to explore in situ fracture hydromechanics. *Journal of geophysical Research: Solid Earth*, *122*, 6046–6066. <https://doi.org/10.1002/2017JB014045>
- Shakas, A., Linde, N., Baron, L., Bochet, O., Bour, O., & Le Borgne, T. (2016). Hydrogeophysical characterization of transport processes in fractured rock by combining push-pull and single-hole ground penetrating radar experiments. *Water Resources Research*, *52*, 938–953. <https://doi.org/10.1002/2015wr017837>
- Shook, G. M. (2001). Predicting thermal breakthrough in heterogeneous media from tracer tests. *Geothermics*, *30*(6), 573–589. [https://doi.org/10.1016/s0375-6505\(01\)00015-3](https://doi.org/10.1016/s0375-6505(01)00015-3)
- Somogyvari, M., Bayer, P., & Brauchler, R. (2016). Travel-time-based thermal tracer tomography. *Hydrology and Earth System Sciences*, *20*(5), 1885–1901. <https://doi.org/10.5194/hess-20-1885-2016>
- Sutton, D. J., Kabala, Z. J., Schaad, D. E., & Ruud, N. C. (2000). The dipole-flow test with a tracer: A new single-borehole tracer test for aquifer characterization. *Journal of Contaminant Hydrology*, *44*(1), 71–101. [https://doi.org/10.1016/s0169-7722\(00\)00083-8](https://doi.org/10.1016/s0169-7722(00)00083-8)
- Tang, D. H., Frind, E. O., & Sudicky, E. A. (1981). Contaminant transport in fractured porous-media - analytical solution for a single fracture. *Water Resources Research*, *17*(3), 555–564. <https://doi.org/10.1029/WR017i003p00555>
- Welty, C., & Gelhar, L. W. (1994). Evaluation of longitudinal dispersivity from nonuniform flow tracer tests. *Journal of Hydrology*, *153*(1–4), 71–102. [https://doi.org/10.1016/0022-1694\(94\)90187-2](https://doi.org/10.1016/0022-1694(94)90187-2)
- Woods, K., & Ortega, A. (2011). The thermal response of an infinite line of open loop wells for ground coupled heat pump systems. *International Journal of Heat and Mass Transfer*, *54*(25–26), 5574–5587. <https://doi.org/10.1016/j.ijheatmasstransfer.2011.07.027>
- Zhou, Q., Oldenburg, C. M., Rutqvist, J., & Birkholzer, J. T. (2017). Revisiting the fundamental analytical solutions of heat and mass transfer: The kernel of multirate and multidimensional diffusion. *Water Resources Research*, *53*, 9960–9979. <https://doi.org/10.1002/2017WR021040>
- Zlotnik, V. A., & Ledder, G. (1996). Theory of dipole flow in uniform anisotropic aquifers. *Water Resources Research*, *32*(4), 1119–1128. <https://doi.org/10.1029/95wr03813>
- Zlotnik, V. A., & Zurbuchen, B. R. (1998). Dipole probe: Design and field applications of a single-borehole device for measurements of vertical variations of hydraulic conductivity. *Ground Water*, *36*(6), 884–893. <https://doi.org/10.1111/j.1745-6584.1998.tb02095.x>